The Astrophysical Journal, 911:81 (19pp), 2021 April 20 https://doi.org/10.3847/1538-4357/abe9b1

Magnetic Fields and Star Formation around H II Regions: The S235 Complex

R. Devaraj[1], D. P. Clemens[2], L. K. Dewangan[3], A. Luna[4], T. P. Ray[1], and J. Mackey[1,5]
[1] Dublin Institute for Advanced Studies, 31 Fitzwilliam Place, Dublin D02XF86, Ireland; dev2future@yahoo.com
[2] Institute for Astrophysical Research, Boston University, 725 Commonwealth Avenue, Boston, MA 02215, USA
[3] Physical Research Laboratory, Navrangpura, Ahmedabad, Gujarat 380009, India
[4] Instituto Nacional de Astrofísica, Óptica y Electrónica, Tonantzintla, Puebla 72840, México
[5] Centre for Astroparticle Physics and Astrophysics (CAPPA), DIAS Dunsink Observatory, Dunsink Lane, Dublin 15, Ireland
Received 2020 November 28; revised 2021 February 18; accepted 2021 February 23; published 2021 April 19

Abstract

Magnetic fields are ubiquitous and essential in star formation. In particular, their role in regulating formation of stars across diverse environments like H II regions needs to be well understood. In this study, we present magnetic field properties toward the S235 complex using near-infrared (NIR) *H*-band polarimetric observations, obtained with the Mimir and POLICAN instruments. We selected 375 background stars in the field through combination of Gaia distances and extinctions from NIR colors. The plane-of-sky (POS) magnetic field orientations inferred from starlight polarization angles reveal a curved morphology tracing the spherical shell of the H II region. The large-scale magnetic field traced by Planck is parallel to the Galactic plane. We identified 11 dense clumps using 1.1 mm dust emission, with masses between 33 and 525 $M_{\odot}$. The clump-averaged POS magnetic field strengths were estimated to be between 36 and 121 μG, with a mean of $\sim$65 μG. The mass-to-flux ratios for the clumps are found to be subcritical with turbulent Alfvén Mach numbers less than 1, indicating a strongly magnetized region. The clumps show scaling of magnetic field strength versus density with a power-law index of 0.52 ± 0.07, similar to ambipolar diffusion models. Our results indicate that the S235 complex is a region where stellar feedback triggers new stars, and the magnetic fields regulate the rate of new star formation.

Unified Astronomy Thesaurus concepts: H II regions (694); Magnetic fields (994); Interstellar magnetic fields (845); Molecular clouds (1072); Starlight polarization (1571); Polarimetry (1278)

Supporting material: machine-readable tables

1. Introduction

The advent of space-based mid-infrared observations has revealed parsec-scale ring-like structures around ionized regions (Churchwell et al. 2006; Deharveng et al. 2010). These are formed by massive stars through their energetic winds, UV ionizing radiation, and expanding H II regions (Zinnecker & Yorke 2007). The resulting turbulent interaction with gas and dust sweeps up the surrounding material and modifies the local magnetic fields (Ferland 2009; Ferrière 2011). Since the magnetic field is generally coupled to the gas, its distribution is critically affected in this process. Furthermore, these dynamics can trigger new generations of stars by collect-and-collapse (Elmegreen & Lada 1977) or by radiation-driven implosion (Bertoldi 1989) processes.

Magnetic fields are believed to play a crucial role in regulating star formation (Mestel & Spitzer 1956; Mouschovias & Ciolek 1999; McKee & Ostriker 2007; Krumholz & Federrath 2019). However, it is unclear how the role of magnetic fields differs with conditions from quiescent molecular clouds to active environments such as H II regions. Stellar feedback of massive stars can compress molecular gas into dense fragments to form new massive stars (Deharveng et al. 2005; Tan et al. 2014), leading to questions regarding the significance of magnetic fields in triggered star-forming conditions. Hence, a detailed study of magnetic field properties is necessary to better understand the dynamics of magnetic fields and how they relate to different star formation properties.

Several observations have revealed young stellar clusters associated with molecular clumps[6] around H II regions (Camargo et al. 2011; Dewangan et al. 2012; Thompson et al. 2012). The clumps are precursors to clusters (Battersby et al. 2010), and thus obtaining magnetic field properties in clumps is critical to assessing their stabilities. The efficiency of the formation of stellar clusters and new stars can be constrained by considering two scenarios. Either the formation is regulated by strong magnetic fields, through the process of ambipolar diffusion (Mouschovias 1991; Mouschovias & Ciolek 1999) or the turbulent gas motions, outflows, and stellar winds provide nonmagnetic support against collapse (McKee & Tan 2003; Padoan et al. 2004; Mackey & Lim 2011). An observational test that can be employed is to compare the relative strengths of the gravitational potential with the magnetic field using the mass-to-flux ratio (Crutcher et al. 2004). Additionally, if changes in magnetic strength have power-law dependency on column densities, it is possible to ascertain the influence of the magnetic field in channeling gas into dense regions.

Theoretical studies indicate that the expansion of an ionized region can lead to more order in the magnetic field around the shell, while the molecular gas is driven to equipartition between thermal, magnetic, and turbulent energies (Krumholz et al. 2007; Arthur et al. 2011). If the ionizing front is perpendicular to the ambient magnetic field, the expansion may be slowed in that direction. A few observational results (e.g., Tang et al. 2009; Santos et al. 2014; Chen et al. 2017) have shown that magnetic field orientations are aligned tangentially to ring-like structures, and the field strength increases in the compressed neutral gas.

While these studies hint at how magnetic fields may be affected by feedback, a systematic study was needed that ranges from parsec to sub-parsec scales and that connects

[6] In this paper, we use the term "clump" to describe a dense region within a cloud with a size of a few parsecs and a mass of $\sim 10^2$–$10^4 M_{\odot}$.

turbulence, magnetic fields, and gravity. In this context, we explored the S235 complex using new polarization observations along with the distributions of dust and molecular gas. The paper is organized as follows. Section 2 gives an introduction to the S235 complex. Section 3 provides new near-infrared (NIR) observational details and assembles relevant archival data products. Section 4 gives descriptions of the analyses and results. This includes selection of background stars, identification of dust clumps, and estimation of the magnetic field properties. Section 5 discusses the implications of the results and the role of magnetic fields. Section 6 contains conclusions and a summary of the study.

2. The S235 Complex

The Sh2-235 (S235) star-forming complex is part of the giant molecular cloud G174+2.5 situated in the Milky Way Perseus spiral arm (Heyer et al. 1996) and contains three known H II regions: "S235 Main" (Sharpless 1959), "S235AB," and "S235C." The kinematic distance to S235 has been considered to be between 1.5 kpc and 1.8 kpc (Evans & Blair 1981; Burns et al. 2015). We use a distance of $1.65^{+0.12}_{-0.10}$ kpc based on the Gaia DR2 (Brown et al. 2018) parallax for the S235 Main ionizing star: BD +35°1201 of O9.5V type (Georgelin et al. 1973). Radial velocity measurements of photospheric lines in BD +35°1201 give an LSR value of -18 km s^{-1} (Kirsanova et al. 2008). Various studies of molecular emission from ^{12}CO,^{13}CO, CS, and NH_3 lines trace structures in the S235 complex over the velocity range -25 to -15 km s^{-1} (Kirsanova et al. 2008, 2014; Chavarría et al. 2014), indicating that the star and molecular material are associated. Dewangan et al. (2016) used radio continuum emission at 1.4 GHz to reveal a spherical distribution of the ionizing radiation. Spitzer mid-infrared (MIR) images (Werner et al. 2004) reveal a spherical shell-like morphology tracing the photodissociation regions (PDRs; see Figure 1). The ionizing star BD +35°1201 appears in projection to be located approximately at the center of the shell.

In addition, the S235AB and S235C regions (smaller, southern part of the complex; see Figure 1) are powered by B0.5V stars (Felli et al. 1997; Bieging et al. 2016). The distance to S235AB has been obtained to be $1.56^{+0.09}_{-0.08}$ kpc from water maser parallax measurements by Burns et al. (2015). Felli et al. (2004) studied these regions with millimeter spectral and continuum observations along with far-infrared data, identifying the presence of a molecular core hosting a young stellar object (YSO) with a bipolar outflow. Using VLA radio centimeter observations and Spitzer data, Felli et al. (2006) suggested that the YSO is the result of star formation triggered by the ionizing wind of the massive star in S235A. Dewangan & Anandarao (2011) identified YSOs in S235 Main and S235AB using Spitzer and NIR photometry. Subsequent studies (see Kirsanova et al. 2014; Dewangan et al. 2016) located these YSOs in association with the molecular gas along the shell and edges of the H II regions (see Figure 1). All of these studies reveal that the S235 complex is dynamic and that triggered star formation is evident around the S235 Main region. However, there has been no study of the magnetic field properties in this complex. Hence, the S235 complex is an ideal laboratory to study the interaction of H II regions, molecular gas, and magnetic fields.

The magnetic field orientations in the S235 complex can be probed using NIR background starlight polarimetry. The dust

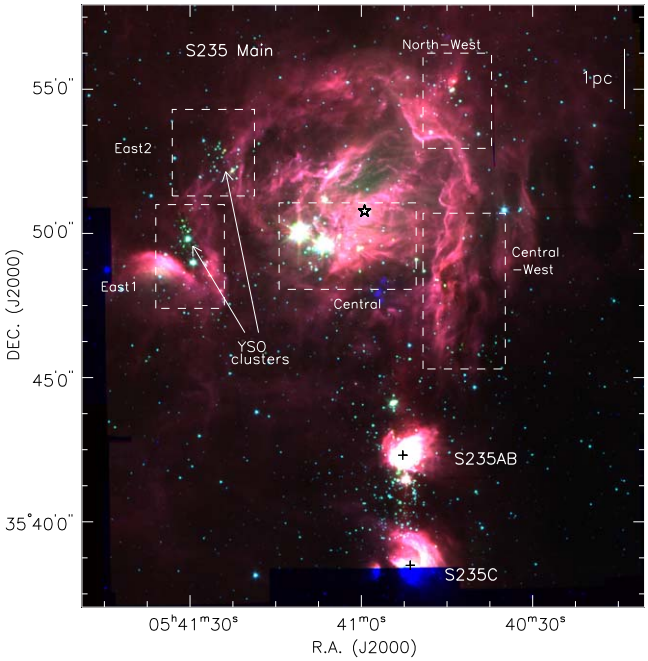

Figure 1. Mid-infrared three-color image of the S235 complex, constructed using Spitzer Infrared Array Camera (IRAC) bands 8 μm (red), 4.5 μm (green), and 3.6 μm (blue; Fazio et al. 2004). The region spans 20′ × 21′, corresponding to a projected physical scale of 9.56 pc × 10.08 pc at a distance of 1.65 kpc. Three separate H II regions, S235 Main, 235AB, and S235C, are identified. The central ionizing O9.5V star for S235 Main is marked by the star symbol, while the ionizing B0.5V stars for S235AB and S235C are shown by cross symbols. Subregions with young stellar object (YSO) clusters identified by Kirsanova et al. (2008) are shown by dashed boxes.

grains in the molecular regions align their long axes perpendicular to the local magnetic field due to radiative torques (Lazarian & Hoang 2007; Andersson et al. 2015). Hence, the light from background stars passing through the dust becomes weakly polarized due to dichroic extinction (Hall 1949; Hiltner 1949). The resulting polarized starlight position angles (PAs) are parallel to the plane-of-sky (POS) magnetic field orientations of the region.

3. Observations and Data Sets

We obtained new polarimetric observations and combined these with archival multiwavelength imaging and spectral data to study the magnetic field properties of the S235 complex. The angular size of the selected region is 20′ × 21′, centered at $\alpha_{2000} = 05^h40^m58^s.9$, $\delta_{2000} = +35°47'25''.7$. This size covered all three H II regions and corresponds to a physical scale of about 9.59 pc × 10.08 pc at a distance of 1.65 kpc.

3.1. Near-infrared Polarization Observations

NIR linear polarimetric observations were obtained in the *H* band (1.6 μm) using two instruments: Mimir (Clemens et al. 2007) and POLICAN (Carrasco et al. 2017; Devaraj et al. 2018a). The Mimir instrument was located on the 1.8 m Perkins telescope outside of Flagstaff, AZ. Mimir used a 1024 × 1024 pixel Aladdin III InSb detector array, operated at 33.5 K. The instrument had a field of view (FOV) of 10 × 10 arcmin^2 and pixel scale of 0.″58. The POLICAN instrument operated on the 2.1 m OAGH telescope in Cananea, Sonora, Mexico. It had a 1024 × 1024 pixel HgCdTe detector with a pixel scale of 0.″32 that provided an FOV of 4 × 4 arcmin^2. Both instruments

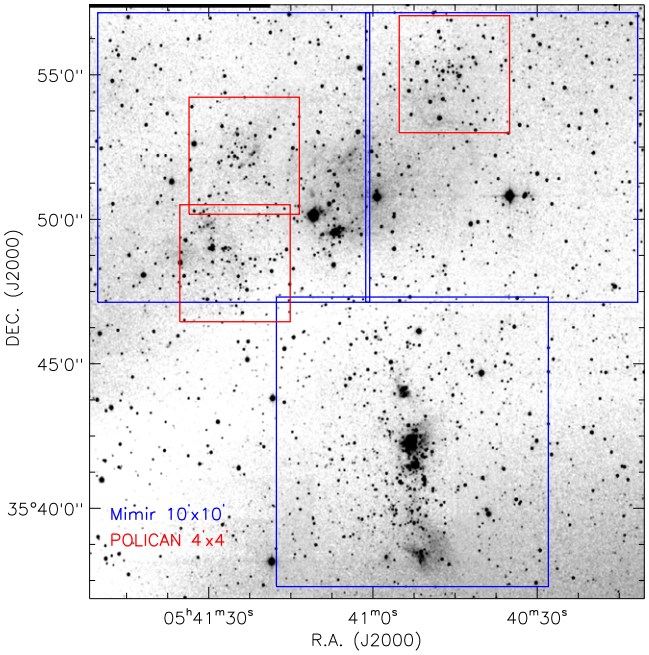

Figure 2. NIR *H*-band image of the S235 complex obtained from Two Micron All Sky Survey (2MASS) data. Colored boxes corresponding to the observed fields are shown. The blue boxes are 10′ fields observed using Mimir. The red boxes are 4′ fields observed using POLICAN.

measured linear polarization by the combination of a half-wave plate (HWP) as the modulator and a fixed wire-grid polarizer as the analyzer. Images obtained through different HWP orientation angles were used to determine the Stokes parameters Q and U for each measured source.

Observations with Mimir were carried out in the H band during 2015 January for seven nights. Three target fields of 10′ were chosen that covered the S235 region, with overlaps of 0.′1 between adjacent fields. The field coverage is shown in Figure 2. Each field was observed in six sky dither positions with images taken at 16 HWP angles. A total of 96 (6×16) images were taken for each field, each with an exposure time of 15 s, for a total integration time of 24 minutes for each field. Each field was observed 14 times totaling 5.6 hr per field. The data reduction and calibration were carried out using the Mimir Software Package: Basic Data Processing (MSP-BDP), and the Photo POLarimetry tool (MSP-PPOL) yielding Stokes parameters Q, U, and polarization values for all of the point sources in the fields. Details of the processes used in the Mimir software package are described in Galactic Plane Infrared Polarization Survey (GPIPS) articles (Clemens et al. 2012a, 2012b).

Observations with the POLICAN instrument focused on reaching finer angular resolutions and signal-to-noise ratios for regions with high stellar density. Three subfields of 4×4 arcmin^2 were observed in the H band during 2017 September. The field coverage is shown in Figure 2. Each set of observations contained 18 sky dither positions at each of four HWP angles (0°, 22.°5, 45°, and 67.°5). Exposure times were 100 s, for a total integration time of 2 hr for the 72 images (18×4) per field. Basic reduction consisted of linearity correction, dark subtraction, flat-fielding, and sky removal. Images were aligned and combined for each HWP angle (see Devaraj et al. 2018b). They were then astrometry-corrected using data from the Two Micron All Sky Survey (2MASS; Skrutskie et al. 2006). Aperture photometry was performed on each source in each of the HWP images. The resulting source intensities were used to compute the Stokes parameters. Descriptions of calibration procedures and polarimetric analyses are given in Devaraj et al. (2018a).

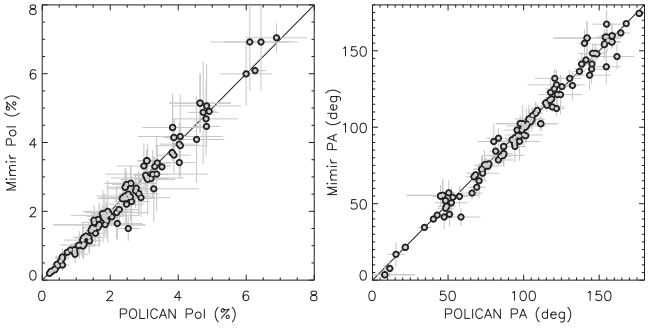

Figure 3. Comparison of Mimir and POLICAN polarization for stars repeated in both fields, having $\sigma_P < 3\%$. The left panel compares degree of polarization and the right panel compares the PAs. In each panel, the solid black line represents equality with unit slope and zero offset.

The polarization percentage (P) and equatorial PA were computed from Stokes parameters Q and U, for both instruments, as follows:

$$P = \sqrt{Q^2 + U^2}, \tag{1}$$

$$PA = \frac{1}{2}\tan^{-1}\left(\frac{U}{Q}\right). \tag{2}$$

The polarization angles are measured from the north-up toward east-left direction. The de-biased degree of polarization (P') was estimated using Ricean correction as prescribed in Wardle & Kronberg (1974):

$$P' = \sqrt{P^2 - \sigma_P^2}, \tag{3}$$

where σ_P is the polarization uncertainty computed by standard error propagation of the corresponding Stokes values and uncertainties (see the Appendix in Devaraj et al. 2018a).

The final results from the observations were data files containing coordinates, brightness magnitudes, Stokes parameters, polarization values, and corresponding uncertainties. Results from both instruments were combined to produce a single set of stellar polarization catalogs. Sources observed multiple times from overlapped regions, and on both instruments, were checked for repeatability.

We found that the Mimir and POLICAN fields have 215 stars in common. Figure 3 compares the polarization values for repeated stars having $\sigma_P < 3\%$. The plot shows excellent correlation with values distributed around the equality line. The mean polarization percentage difference of the two sets was $0.20\% \pm 0.06\%$ with a standard deviation of $0.4\% \pm 0.1\%$. The mean PA difference was $0.^\circ6 \pm 0.^\circ4$ with a dispersion of $3.^\circ8 \pm 0.^\circ7$. In order to retain only one value of each repeated star for the final data set, we chose the value having the highest polarization signal-to-noise ($P_{S/N} = P'/\sigma_P$) between both measurements. The selected stars were added to the combined set containing unique Mimir and unique POLICAN stars. To favor the most reliable polarimetric data, we retained only those sources meeting the criteria $P_{S/N} > 1$ and $\sigma_P < 3\%$. This resulted in 623 sources with reliable stellar polarization values.

Table 1 lists the polarimetric properties of the 623 stars in the S235 field. The table columns are ordered as follows: star ID,

Table 1
Polarimetric Properties of the 623 Stars in the S235 Complex

ID	R.A. (J2000)	Decl. (J2000)	H Band (mag)	P' (%)	PA (deg)	Q (%)	U (%)
1	85.10488	35.90900	11.83 (0.01)	0.4 (0.2)	142 (12)	0.1 (0.1)	−0.4 (0.2)
2	85.10931	35.89397	15.12 (0.03)	6.2 (2.2)	159 (10)	5.0 (2.3)	−4.2 (2.2)
3	85.11411	35.91162	13.58 (0.03)	1.0 (0.6)	10 (18)	1.2 (0.6)	0.4 (0.6)
4	85.11484	35.84210	12.25 (0.01)	1.1 (0.2)	130 (5)	−0.2 (0.1)	−1.0 (0.2)
5	85.11559	35.87341	15.09 (0.03)	3.2 (2.4)	133 (21)	−0.3 (2.3)	−4.0 (2.4)
6	85.12303	35.73406	14.93 (0.02)	4.1 (2.0)	132 (14)	−0.4 (2.0)	−4.5 (2.0)
7	85.12359	35.93396	11.94 (0.01)	0.4 (0.2)	9 (12)	0.5 (0.2)	0.1 (0.2)
8	85.12410	35.64257	12.28 (0.01)	0.7 (0.6)	131 (26)	−0.1 (0.6)	−1.0 (0.6)

Note. Only a portion of this table is shown here to demonstrate its form and content. A machine-readable version of the full table is available. Uncertainties are given in parentheses.

(This table is available in its entirety in machine-readable form.)

Table 2
Archival Data Sets Adopted in This Work

Survey	Wavelength(s)	Resolution	Reference
UKIRT Infrared Deep Sky Survey (UKIDSS)	0.88–2.2 μm	$\sim 0\farcs8$	Lawrence et al. (2007)
Two Micron All Sky Survey (2MASS)	1.25–2.2 μm	$\sim 2\farcs5$	Skrutskie et al. (2006)
Spitzer IRAC GTO program ID:201	3.6, 4.5, 5.8, 8.0 μm	$\sim 2''$	Fazio et al. (2004)
Planck dust polarization data	850 μm	$\sim 5'$	Planck Collaboration I (2016)
Bolocam Survey extended to outer Galaxy	1.1 mm	$\sim 33''$	Ginsburg et al. (2013)
Extended Outer Galaxy Survey ^{13}CO ($J = 1$–0)	2.7 mm	$\sim 45''$; velocity 0.21 km s^{-1}	Brunt (2004)

equatorial coordinates R.A. and decl., Mimir or POLICAN H-band magnitudes, de-biased polarization percentage, equatorial PA, and the equatorial Stokes Q and U parameters. The uncertainties are given in parentheses.

3.2. Planck Polarized Dust Emission

The Planck all sky survey data (Planck Collaboration I 2016) were used to obtain a map of polarized dust emission toward the S235 complex. We retrieved the Intensity I, Stokes Q, and U sky maps observed with the High Frequency Instrument at 353 GHz. The procedures of map-making, calibration, and corrections are described in Planck Collaboration VIII (2016). We smoothed the maps from an initial angular resolution of 5′–6′ to increase the signal-to-noise ratio and to minimize beam depolarization effects. The intensity and polarization maps were converted from the $K_{\rm CMB}$ temperature scale to MJy sr^{-1} using the unit conversion and color correction factor of 246.54. The intensity map was also subtracted for the Galactic zero level offset of 0.0885 MJy sr^{-1} (Planck Collaboration VIII 2016). The corrected maps of Stokes parameters were analyzed using the surface brightness of each pixel to calculate the polarization values, as given in Equations (1) and (2). This resulted in a linear polarization map of dust emission integrated along the line of sight (LOS). More details on polarization analysis is presented in Planck Intermediate Results XXXIV (2016). The electric field polarization PAs were rotated by 90° to yield POS magnetic field orientations. The rotated polarization angles are represented in equatorial coordinates and measured from the north-up toward east-left direction.

3.3. Archival Data Sets

Additional archival data sets, ranging from NIR to radio wavelengths, were used in our study. NIR photometry was obtained from 2MASS and UKIDSS data to estimate the visual extinction for polarization stars. MIR images, which reveal PDRs were obtained from the Spitzer Infrared Array Camera (IRAC) guaranteed time observations (GTOs; Fazio et al. 2004). Dust continuum emission at 1.1 mm was obtained from the Bolocam Galactic Plane Survey, version 2.1 (Aguirre et al. 2011; Ginsburg et al. 2013) with extension to the outer Galaxy. These data were used to identify molecular clumps and estimate H_2 column densities. ^{13}CO molecular line data ($J = 1 - 0$, 110.2 GHz) with an rms sensitivity of ∼0.13 K (Jackson et al. 2006) were obtained from the Extended Outer Galaxy Survey (Brunt 2004) taken using the FCRAO telescope. The molecular data were used to find gas velocity properties. Table 2 summarizes the survey wavelengths and resolutions of the data sets.

4. Analyses

4.1. Selection of Background Stars

Since the magnetic field inside the S235 complex was to be probed using the polarimetry of background stars, it is important to identify foreground and background stars among all 623 sources observed. The selection of background stars involved three steps. Step 1: identification and exclusion of YSOs using the NIR color–color diagram. Step 2: use of Gaia distances to classify foreground and background stars for the stars with Gaia matches. Step 3: stars without Gaia distances

had their extinctions analyzed to discern their foreground or background natures.

4.1.1. Identification of YSOs

The reddening and polarization of stars is related to the extinction by dust in clouds and in the diffuse interstellar medium (Martin et al. 1992; Whittet et al. 1992). However, YSOs and NIR-excess sources exhibit polarization due to reflected/scattered light from their circumstellar disks/envelopes and surrounding nebulosity (Bastien 1996; Tamura et al. 2006). Hence, their polarizations do not trace magnetic field directions, and such sources need to be excluded.

Dewangan & Anandarao (2011) and Chavarría et al. (2014) presented a catalog of YSOs in the S235 complex identified using NIR and Spitzer data. Their study lists different classes of YSOs, but they do not properly account for YSO contaminations. Examination of their catalog shows that many of the YSOs reveal NIR colors resembling giant and main-sequence (MS) stars. Hence, we did not use these catalogs for YSO identification and performed separate analyses using NIR data.

The NIR color–color diagram provides a useful technique for identifying populations of YSOs (Lada & Adams 1992). Using the unreddened loci for MS, giant, and young stars, we can classify sources based on their color excess. The loci can be extended to account for reddening using the NIR extinction law (Mathis 1990). Within the $(J-H)$ versus $(H-K)$ color–color diagrams, the distributions of sources typically fall into three regions, designated here as "F," "T," and "P" (see Sugitani et al. 2002; Mallick et al. 2012). The "F" region contains field stars that include MS, giant, and Class III (diskless) YSOs. The "T" region contains classical T Tauri stars (CTTSs; Class II protostars). The "P" region contains Class I protostars and Herbig Ae/Be stars with large NIR excesses.

The 623 polarimetric stars were matched to the 2MASS point-source catalog (Skrutskie et al. 2006) to yield 559 stars with J, H, and K band photometry. The stars with no 2MASS magnitudes were matched with the UKIDSS catalog (Lawrence et al. 2007) to obtain an additional 53 stars with NIR photometry. The UKIDSS magnitudes were calibrated to the 2MASS system as described in Hodgkin et al. (2009). The combination of 2MASS and UKIDSS matched sources resulted in a total of 612 polarimetric stars having magnitudes in all three J, H, and K bands. Figure 4(A) shows the $E(J-H)$ versus $E(H-K)$ color–color diagram for this sample of 612 stars. The loci of curves for MS stars and giants were taken from Bessell & Brett (1988) and converted to the 2MASS system using equations from Carpenter (2001). The CTTS loci was taken from Meyer et al. (1997). These curves were then extended using reddening vectors drawn from the tip (spectral type M4) of the giant branch (blue line), from the base (spectral type A0) of the MS branch (red line), and from the tip of the intrinsic CTTS line (cyan line) using extinction ratios $A_J/A_V = 0.265$, $A_H/A_V = 0.155$, and $A_K/A_V = 0.09$, obtained from Cohen et al. (1981).

In Figure 4(A), 38 sources were found to fall within the "T" and "P" regions. These sources were classified as YSOs and are shown separately in Figure 4(B). There were also 14 sources having color excesses that did not fall into any classification. These sources, along with the YSOs, were excluded from subsequent analyses.

The remaining sample of 560 stars fell in the "F" region, indicating that they are most likely normal MS and giant stars. These stars should be free from intrinsic polarization, and their observed polarizations are due to dichroic extinction. The 560 sources were retained for this study and include foreground stars and background stars to the S235 complex.

4.1.2. Gaia Distances

The Gaia collaboration DR2 provides parallax values for sources as faint as 20 mag in the G band. Bailer-Jones et al. (2018) provided a catalog of distance estimates for the sources in Gaia DR2. Their inferred distances are the modes of the posterior probability density functions from the measured parallax values, obtained using a varying distance prior. From the Bailer-Jones et al. (2018) catalog, we retrieved distances and astrometric information for the sources within the S235 field. We cross-matched the 560 field stars to Gaia data, using a match radius of $2''$. In total, 382 stars from the sample were found to have Gaia matches.

Figure 5 plots color excess against distance for the 382 Gaia matched stars. The solid black vertical line represents the 1.65 kpc distance to the S235 complex. The stars show a positive correlation of color excess with distance. The distribution has a step-wise trend with the step centered near the distance of 1.65 kpc. A horizontal solid black line of $E(H-K) = 0.3$ is shown to represent the average of the step, distinguishing regions of low and high color excess. The low color excess stars mostly have distances less than 1.65 kpc. Stars with $E(H-K) > 0.3$ mainly show distances greater than 1.65 kpc.

The stellar distribution in Figure 5 was interpreted to contain three distinct populations of stars, namely: foreground, background, and stars associated with, or embedded in, the S235 complex. The foreground stars were considered those with distances less than 1.5 kpc. Of the 382 stars, 182 stars fell into this category and are shown as black symbols in Figure 5. The background stars were those having distances greater than 1.9 kpc. A total of 160 stars met this criterion and are shown as dark blue symbols in Figure 5. The background stars predominantly have a color excess of $E(H-K) > 0.3$, indicating that they are highly extincted.

The stars associated with the S235 complex are the sample located near the distance of 1.65 kpc, with a range of 1.5–1.9 kpc. Although this distance range is much larger than typical cloud sizes, we consider the stars in it to be associated with the S235 complex given the distance uncertainties of the Gaia DR2 data. The stars that fell in the associated region are shown as cyan symbols in Figure 5. This sample includes stars that lie outside the S235 complex and stars that are embedded in it. The embedded stars are likely the subset that are moderately extincted, with color excesses of $0.3 < E(H-K) < 0.6$. There were 40 stars satisfying this condition, and they were deemed embedded. A red dashed box in Figure 5 is shown to represent the region containing the embedded stars. The 160 background stars and the 40 embedded stars formed a total of 200 Gaia matched stars for use in the magnetic field analyses.

4.1.3. Stellar Extinction

The 178 field stars that did not have Gaia matches were examined further to classify their locations based on their extinction values. Since extinction is attributed to the amount of intervening dust in the LOS of a star, it can be used to classify stars as being either foreground or background to a cloud (Hoq et al. 2017; Santos et al. 2017).

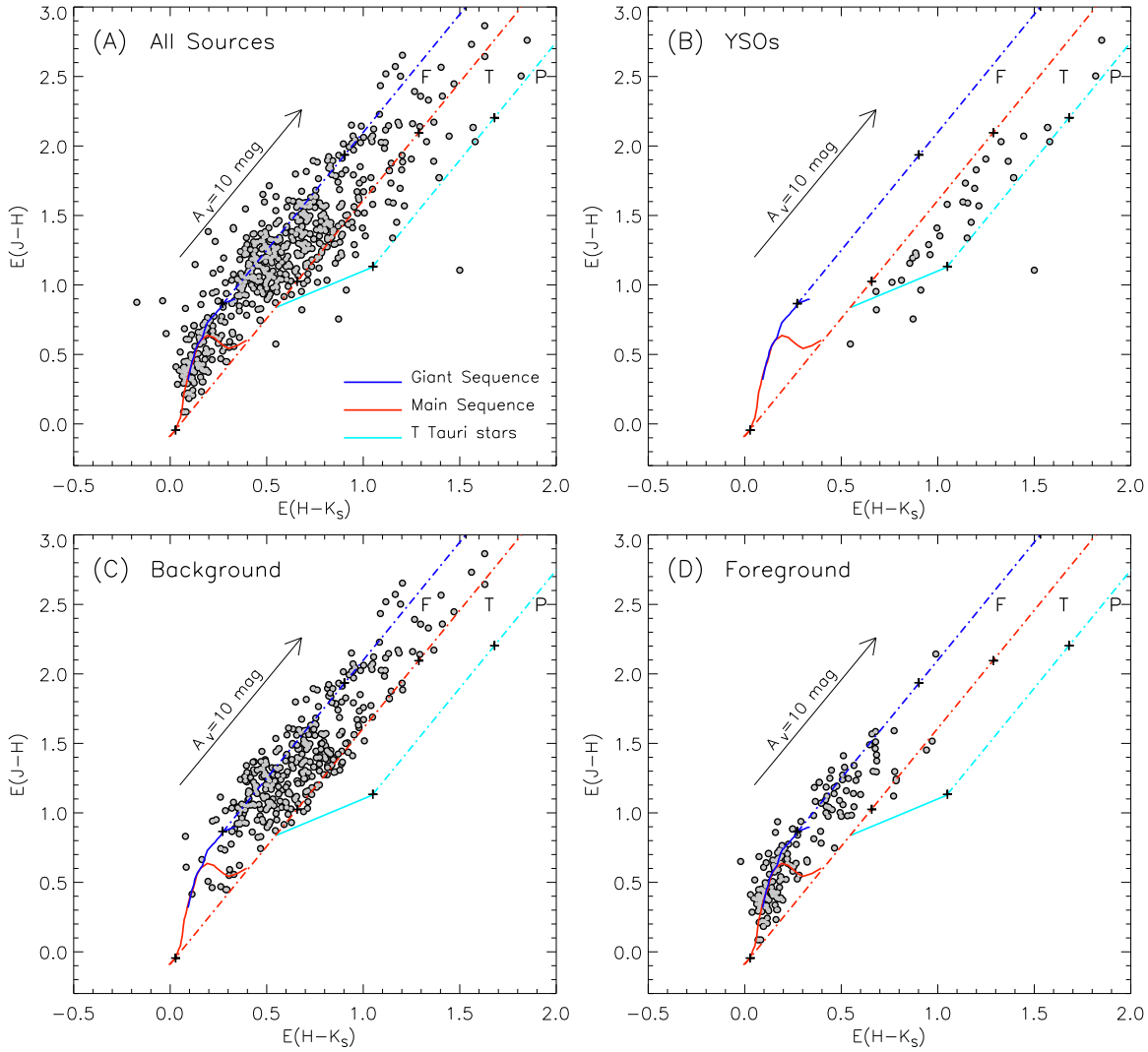

Figure 4. NIR color–color diagram ($J-H$) vs. ($H-K$) for the 612 polarimetric sources in the S235 complex. The solid curves represent the unreddened locus of MS (blue), giant (red), and T Tauri stars (cyan). The loci are extended as three parallel dashed lines to represent reddening. An extinction arrow of 10 mag is shown for reference. The diagrams are classified into three regions: "F," "T," and "P" (see the text). Panel (A) shows the distribution of all 612 polarimetric sources that matched to the 2MASS and UKIDSS catalog. Panel (B) shows the colors of the 38 YSOs falling within the "T" and "P" regions. Panel (C) shows the colors of the 375 background stars identified using Gaia distances and extinction. Panel (D) shows the colors of the 185 foreground stars from the remaining sample.

The stellar extinction values can be calculated using the color excess obtained from 2MASS and UKIDSS magnitudes. The ratio of the total to selective extinction R is given as $R_{XY}=A_V/E(X-Y)$. The values of R in the NIR are $R_{HK}=15.87$, $R_{JH}=9.35$, and $R_{JK}=5.89$ (Rieke & Lebofsky 1985). Taking into account the intrinsic colors (mean intrinsic color was determined to be ∼0.15 from a nearby control field), the relation for visual extinction to NIR color excess is written as:

$$A_V = 15.87 \times [(H-K_s) - 0.15]. \quad (4)$$

The estimated extinction values for all 560 field stars are plotted against their H-band magnitudes in Figure 6(A). The Gaia matched embedded and background stars are shown by the blue symbols, whereas the Gaia matched foreground stars are shown by the black symbols. The 178 Gaia unmatched stars are shown by the red symbols. Most of the Gaia matched stars are distributed across both low and high-extinction zones but favor brighter H-band magnitudes. The Gaia unmatched stars are found predominantly at high-extinction zones and at fainter H-band magnitudes.

Clemens et al. (2020) compared extinction values for GPIPS stars with and without Gaia distances. They showed that the GPIPS stars not matching the Gaia sample were the most extincted of all, reaching A_V values up to 30 mag. To determine which of the Gaia unmatched stars are background to the S235 complex, we compared their extinctions with the properties of Gaia matched background stars.

In Figure 5, the Gaia background stars predominantly show a color excess of $E(H-K)>0.3$, or $A_V>2.4$ mag, using Equation (4). A dashed horizontal line is shown in Figure 6 to represent $A_V=2.4$ mag. More than 97% of Gaia unmatched stars have $A_V>2.4$ mag, indicating that they are mostly likely embedded or background stars.

A histogram of A_V values is shown in Figure 6(B) and reveals two distinct populations of stars. There is an initial increase in extinction seen as a small bump up to $A_V=2.4$ mag. This contribution is due to the dust in the interstellar medium being revealed by foreground stars. Beyond $A_V=2.4$ mag, there is a rise in A_V due to extinction by dust in the cloud. Based on these results and from comparison with Figure 5, we

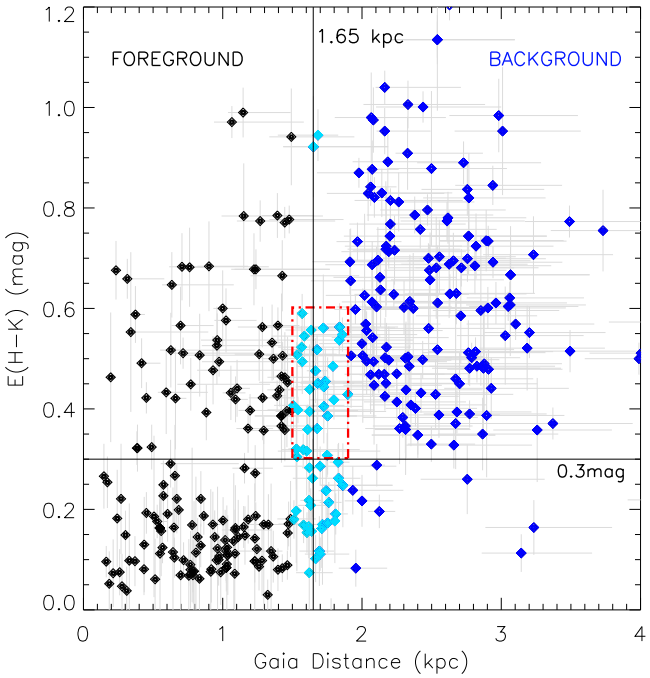

Figure 5. Plot of color excess $E(H-K)$ against distances for the 382 Gaia matched stars. The solid black vertical line represents the 1.65 kpc distance to the S235 complex. The solid horizontal line shows a color excess of 0.3 mag. The foreground stars are shown as black symbols. The background stars are shown as dark blue symbols. The stars associated with the S235 complex, ranging in distance from 1.5 to 1.9 kpc, are shown as cyan symbols. A red dashed box covering $0.3 < E(H-K) < 0.6$ is shown to represent the region containing embedded stars in the S235 complex.

infer that Gaia unmatched stars having $A_V > 2.4$ mag are embedded or behind the cloud. This analysis resulted in 175 Gaia unmatched stars being classified as embedded or background. These 175 stars were merged with the Gaia matched embedded and background stars (200 stars) to obtain a total of 375 stars suitable for magnetic field analyses. The 375 stars are shown in NIR color–color diagram in Figure 4(C).

4.1.4. Accounting for Foreground Polarization

Since the dust foreground to the S235 complex contributes its polarization signal to that of every background star, those contributions should be removed from the background star polarizations prior to magnetic field analyses. We assumed a uniform layer of interstellar dust in front of the S235 complex. This assumption is reasonable as there is only one molecular velocity component along the LOS (the S235 component; see Section 4.3) and there is no other cloud either foreground or background to the S235 complex.

Based on the previous steps of embedded and background star selection, the remaining 185 field stars (182 Gaia matched and 3 Gaia unmatched) were classified as foreground, and are shown in the NIR color–color diagram in Figure 4(D). Of these 185 stars, we selected only the subsample having a low color excess of $E(H-K) < 0.3$, to remove any bias from high-extinction foreground stars. We find the average polarization of this foreground subsample to be ∼0.3%. Using the individual Stokes values of foreground stars, we estimated the weighted mean Stokes value of the foreground contribution. The values are $Q_{\rm fg} = 0.19\% \pm 0.04\%$ and $U_{\rm fg} = -0.11\% \pm 0.03\%$. These were subtracted from the Stokes values of background stars to produce foreground-corrected Stokes values as $Q_{\rm cor} = Q - Q_{\rm fg}$ and $U_{\rm cor} = U - U_{\rm fg}$. The de-biased degree of polarization and PAs were then calculated using Equations (1)–(3).

The distributions of 375 foreground-corrected embedded and background star polarizations are shown as histograms in Figure 7. To represent the histograms accurately and to account for value uncertainties, each star value and its uncertainty were replaced by Gaussian probability densities, accumulated, and placed into the corresponding histogram bins. The red solid lines in Figure 7 represent the net Gaussian probability density distribution for the polarization values. The degree of polarization for the sample ranges between 1% and 10% with a mean of $2.5\% \pm 0.2\%$ and a standard deviation of $1.4\% \pm 0.1\%$. The mean polarization value is similar to the typical values of NIR dust polarization in molecular clouds (Chapman et al. 2011; Clemens et al. 2020) and larger than the average interstellar polarization of ∼0.5% in the H band (Martin et al. 1992; Whittet et al. 1992). About 25% of the S235 stars exhibit a polarization percentage greater than 4% and so could be probing more extincted regions of the cloud. The polarization efficiency in the S235 complex is discussed in Section 5.1. The polarization angles have a mean value of 114° and a dispersion of about 22°. These final polarization values represent the POS magnetic field orientations and are shown in Figure 8 as pseudo-vectors on the Spitzer mid-infrared image of the S235 complex.

Table 3 lists the polarimetric and photometric properties of the 375 foreground-corrected embedded and background stars. The table columns are ordered as follows: star ID, equatorial coordinates R.A. and decl., de-biased polarization percentage, equatorial PA, 2MASS, or UKIDSS magnitudes in the J, H, and K bands, visual extinction, and Gaia DR2 distances from Bailer-Jones et al. (2018) with their low and high values.

4.2. Clump Identification and Clump Properties

Molecular clumps are cold, high-density structures often associated with star or stellar cluster formation (Evans 1999) and can be traced through their dust continuum emission. Determining clump physical properties and studying their magnetic field properties are needed to establish the dynamics of triggered star formation at smaller scales. We used Bolocam 1.1 mm (Ginsburg et al. 2013) data to identify dense and massive clumps around the S235 H II region. Figure 9 shows the distribution of dust emission in blue contours and identifies the clumpy nature of the S235 complex.

The Bolocam Galactic Plane survey (Aguirre et al. 2011) used the customized algorithm Bolocat (Rosolowsky et al. 2010) to identify clumps and to generate catalogs of sources. The algorithm identified sources based on their signal compared to a local estimate of the noise. Regions with high signals are then subdivided into individual sources, based on the presence of local maxima within the region. These sources are expanded to include adjacent low-significance signals using a seeded watershed algorithm (Yoo 2004). The properties of the sources are measured using the moments of the emission assigned to each of the identified sources.

We applied the Bolocat algorithm to the S235 data, using a detection threshold of 3σ and an expanding parameter of 1.5σ, for an estimated σ of 0.035 Jy/beam. This produced 11 clumps having peak emission greater than 10σ. Figure 10 displays the identified clumps with their boundaries. Overplotted are embedded and background star polarization vectors representing magnetic field orientations. The 11 clumps span sufficient

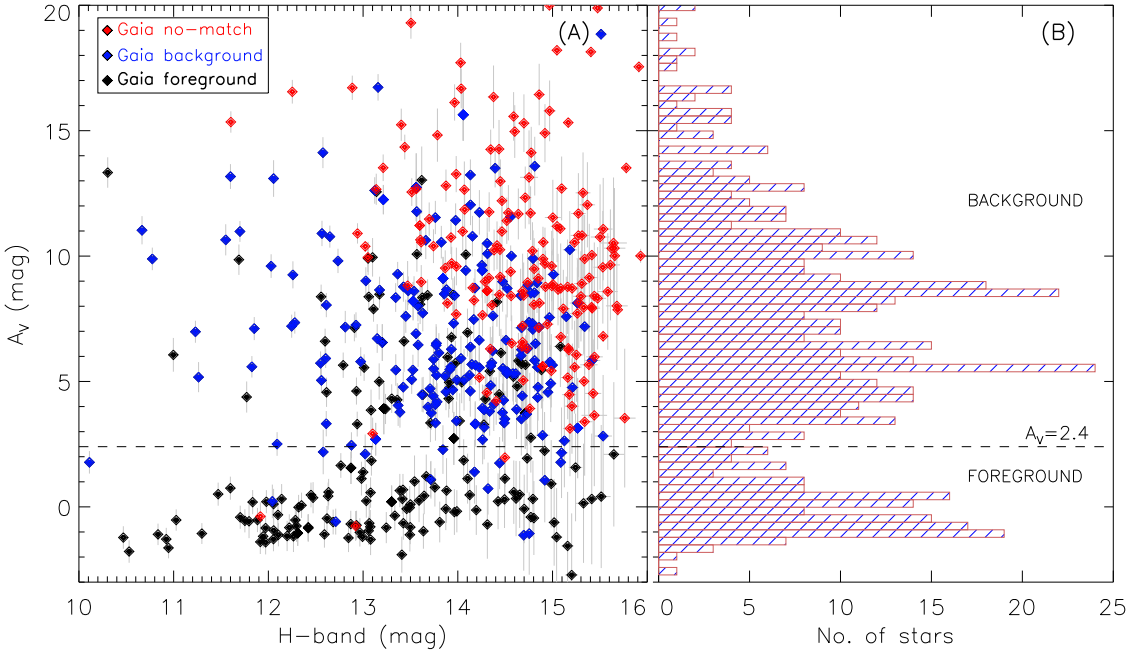

Figure 6. Panel (A) compares extinction values for the 560 field stars against their H-band magnitudes. The Gaia matched embedded and background stars are shown by the blue symbols, whereas the Gaia matched foreground stars are shown by the black symbols. The Gaia unmatched stars are shown by the red symbols. Panel (B) shows the histogram distribution of the same extinction values. In both panels, the dashed horizontal line represents $A_V = 2.4$ mag, which corresponds to $E(H-K) = 0.3$ mag, as shown in Figure 5.

solid angles to encompass many starlight measurements each. The effective radii $R_{\rm eff}$ of the clumps were estimated using a two-dimensional circular Gaussian fit to each clump. The Gaussian fit was then deconvolved by the Bolocam beam. The resulting values for $R_{\rm eff}$ are listed in Table 4 and range from 0.26 pc to 0.75 pc, with a mean radius of 0.5 pc.

4.2.1. Clump Masses and Column Densities

The dust continuum emission offers a reliable tracer of the clump masses due to the low optical depths of the dust (Johnstone & Bally 2006). The total gas and dust mass, also called the isothermal mass $M_{\rm iso}$, (due to the simplifying assumption that the dust can be characterized by a single temperature) within each molecular clump can be derived from the integrated 1.1 mm flux using the following equation (Hildebrand 1983):

$$M_{\rm iso} = \frac{S_\nu\, D^2}{B_{(\nu,T_d)}\, \kappa_\nu}\ ({\rm g}), \tag{5}$$

where S_ν is the integrated 1.1 mm flux in janskys, D is the distance (1.65 kpc), $B_{(\nu,T_d)}$ is the Planck function at the dust temperature $T_d = 20$ K (Kirsanova et al. 2014), and $\kappa_\nu = 0.0114\ {\rm cm^2\ gm^{-1}}$ is the dust absorption coefficient for a gas-to-dust ratio of 100 (Enoch et al. 2006; Bally et al. 2010). Adopting these values, the equation simplifies to $M_{\rm iso} = 13.07 \times S_\nu D^2\ (M_\odot)$.

The inferred clump masses range from 33 to 525 $M_\odot$ and are presented in Table 4. The uncertainties were estimated by propagating the error values of integrated flux. The total gas mass of all 11 clumps is ∼1520 $M_\odot$. Kirsanova et al. (2014) estimated gas masses using NH_3 spectral lines, for a few subregions in the S235 complex. We find good agreement with their mass estimates, with a comparative mass ratio of 1.05 ± 0.07 between Kirsanova et al. (2014) values and this work.

The column densities of the clumps are essential for assessing the effects of self-gravity and magnetic fields. We calculate two measures of the column density: the integrated column density $N(H_2)^{\rm int}_{1.1}$, and the average column density $N(H_2)^{\rm avg}_{1.1}$. The integrated column density is given by the following equation (Bally et al. 2010):

$$N(H_2)^{\rm int}_{1.1} = \frac{S_\nu}{B_{(\nu,T_d)}\, \kappa_\nu\, \mu_{H_2}\, m_{\rm H}\, \Omega_{\rm beam}} ({\rm cm^{-2}}) \tag{6}$$

where S_ν, $B_{(\nu,T_d)}$, and κ_ν are defined in Equation (5). μ_{H_2} is the mean molecular weight per hydrogen molecule considered to be 2.8 (Kauffmann et al. 2008), $m_{\rm H}$ is the mass of a single hydrogen atom in grams, and $\Omega_{\rm beam}$ is the beam solid angle given by $\left(\frac{\sqrt{\pi}\ {\rm FWHM}}{206265 \times \sqrt{4 \ln 2}}\right)^2$. $\Omega_{\rm beam}$ was calculated to be 2.9×10^{-8} sr for the Bolocam FWHM of 33″. Adopting these values and for a dust temperature $T_d = 20$ K, the integrated column density equation reduces to $N(H_2)^{\rm int}_{1.1} = 2.014 \times 10^{22} S_\nu\ ({\rm cm^{-2}})$.

The average column density for each clump can be calculated from its isothermal mass within a given aperture as (Dunham et al. 2011):

$$N(H_2)^{\rm avg}_{1.1} = \frac{M_{\rm iso}}{\mu_{H_2}\, m_{\rm H}\, \pi\, R^2_{\rm eff}}\ ({\rm cm^{-2}}), \tag{7}$$

where $M_{\rm iso}$, μ_{H_2}, $m_{\rm H}$, and $R_{\rm eff}$ are the same as defined earlier.

The estimated values of integrated and average column densities are listed in Table 4. The quantity $N(H_2)^{\rm avg}_{1.1}$ is smaller than $N(H_2)^{\rm int}_{1.1}$ since it is averaged over the entire area of the clump. The $N(H_2)^{\rm avg}_{1.1}$ values range from 2.6×10^{21} cm^{-2} to 1.3×10^{22} cm^{-2}, with a mean of $6.9 \pm 0.3 \times 10^{21}$ cm^{-2} and a standard deviation of $2.5 \pm 0.2 \times 10^{21}$ cm^{-2}. These are

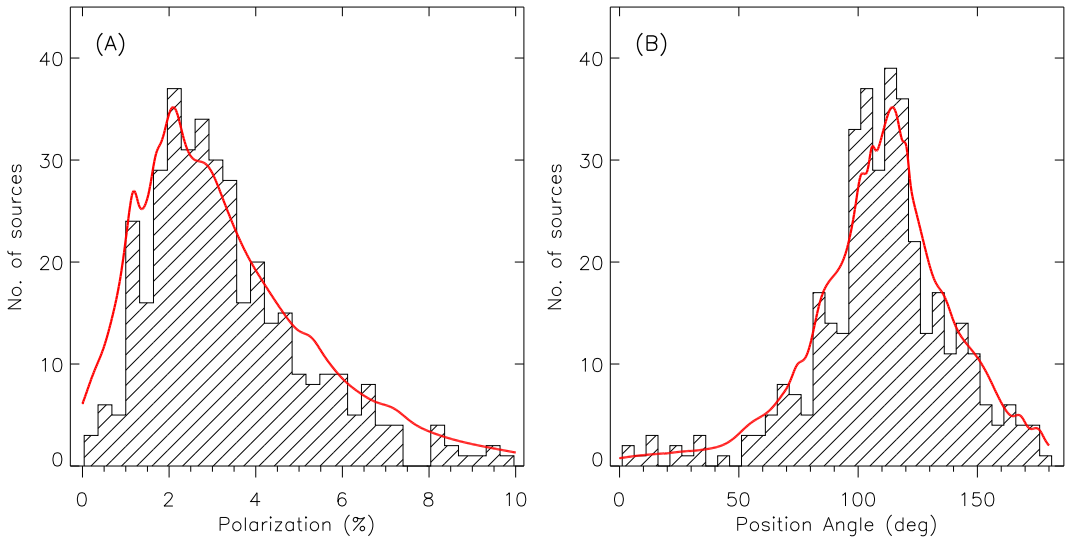

Figure 7. Histograms of polarization values for the 375 foreground-corrected embedded and background stars. Panel (A) shows the distribution of de-biased polarization percentage. The mean polarization value for the sample of stars was 2.5% ± 0.2% with a standard deviation of 1.4% ± 0.1%. Panel (B) shows the polarization PAs. The mean PA was 114° ± 4° with a dispersion of 22° ± 1°. The red solid line in each panel represents the Gaussian probability density distribution for the polarization values, considering the uncertainties, and placed into corresponding histogram bins.

consistent with the typical values for clumps in Galactic molecular clouds (Dunham et al. 2011).

Table 4 lists the derived physical properties of the 11 clumps. The table columns are ordered as follows: clump ID, equatorial coordinates R.A. and decl. obtained at the centroids of the clumps, clump effective radius, integrated flux, isothermal mass, virial mass (see Section 4.5.3), and the average column density.

4.3. Molecular Cloud Distribution

We used the optically thin ^{13}CO (J = 1–0) line data (Brunt 2004) to obtain the molecular cloud properties. The analysis of the ^{13}CO channel maps revealed that emission from the S235 complex was associated in the velocity range −25 to −15 km s^{-1} (Kirsanova et al. 2008; Dewangan & Ojha 2017). The spatial distribution of the molecular gas was traced by integrating the intensity of the ^{13}CO spectra over that velocity range. Figure 9 shows the distribution of ^{13}CO integrated emission as grayscale contours. The molecular gas traces a shell-like envelope around the S235 Main region with a cavity toward the north. The gas is distributed inhomogeneously and shows several dense condensations. The peak emission for both the dust and the molecular data shows close association (see Figure 9), with the average dust to gas peaks offset by only 28″ ± 6″. This indicates that the identified dust clumps correspond to denser molecular gas.

Studies by Kirsanova et al. (2008, 2014) compared emission from CS(2–1) (a biased tracer of dense gas) and ^{13}CO(1–0) (a less biased tracer of all molecular gas) to show that the S235 molecular cloud is separated into different phases, depending on the component velocity. They identified three main phases: undisturbed quiescent gas ($-18\,\mathrm{km\,s^{-1}} < V_{\rm LSR} < -15\,\mathrm{km\,s^{-1}}$), gas affected by the expanding H II region ($-21\,\mathrm{km\,s^{-1}} < V_{\rm LSR} < -18\,\mathrm{km\,s^{-1}}$), and gas expelled from vicinities of the embedded young stars ($-25\,\mathrm{km\,s^{-1}} < V_{\rm LSR} < -21\,\mathrm{km\,s^{-1}}$). Based on this, they suggested the H II region in the S235 Main is expanding largely toward the observer. They further divided the complex into different subregions, based on the locations of young stellar clusters, namely: East1; East2; Central; North-West; and Central-West. These subregions are highlighted by the dashed boxes in Figure 9.

In order to estimate the magnetic field properties in the diffuse part of the S235 cloud, we selected two circular regions (D1 and D2; see Figure 9) that lacked any overlap with the dust clumps. The regions were chosen based on areas with a high density of polarization stars covering both S235 Main and S235AB. The radius of each circular region was set equal to the mean effective radius of the 11 clumps. Since the diffuse regions lacked any prominent dust emission, we calculated their hydrogen column densities using ^{13}CO data. We applied the column density equation given by Simon et al. (2001):

$$N(\mathrm{H_2})_{\rm CO} = 4.92 \times 10^{20} T_{\rm mb} \Delta v \ \ (\mathrm{cm^{-2}}), \tag{8}$$

where $T_{\rm mb}$ is the peak antenna temperature in K, and Δv is the velocity FWHM line width in km s^{-1}, both obtained from the ^{13}CO spectra, corrected for main-beam efficiency of 0.48 (Jackson et al. 2006). The average column density $N(\mathrm{H_2})^{\rm avg}_{\rm CO}$ for the diffuse regions was calculated as the mean of the column densities for all pixels in each region. The $N(\mathrm{H_2})^{\rm avg}_{\rm CO}$ for D1 and D2 were 2.1×10^{21} cm^{-2} and 3.7×10^{21} cm^{-2}, respectively.

4.4. Magnetic Field Strengths

The POS magnetic field strength can be estimated by the method proposed by Davis (1951) and Chandrasekhar & Fermi (1953), hereafter the DCF-method. This method relies on the assumption of equipartition between gas turbulent and mean magnetic energies. Hence, turbulent gas motions (dispersion in gas velocity) will lead to irregularities in magnetic field orientations that can be sensed via dispersions in polarization PAs. Following DCF, the POS magnetic field strength ($B_{\rm pos}$) is estimated as

$$B_{\rm pos} = Q\sqrt{4\pi\rho}\,\frac{\sigma_v}{\delta\theta}\ \ (\mu\mathrm{G}), \tag{9}$$

where ρ is the gas mass volume density (in g cm^{-3}), σ_v is the gas velocity dispersion (in cm s^{-1}), $\delta\theta$ is the PA dispersion (in radians), and Q is a scaling factor. Several simulations

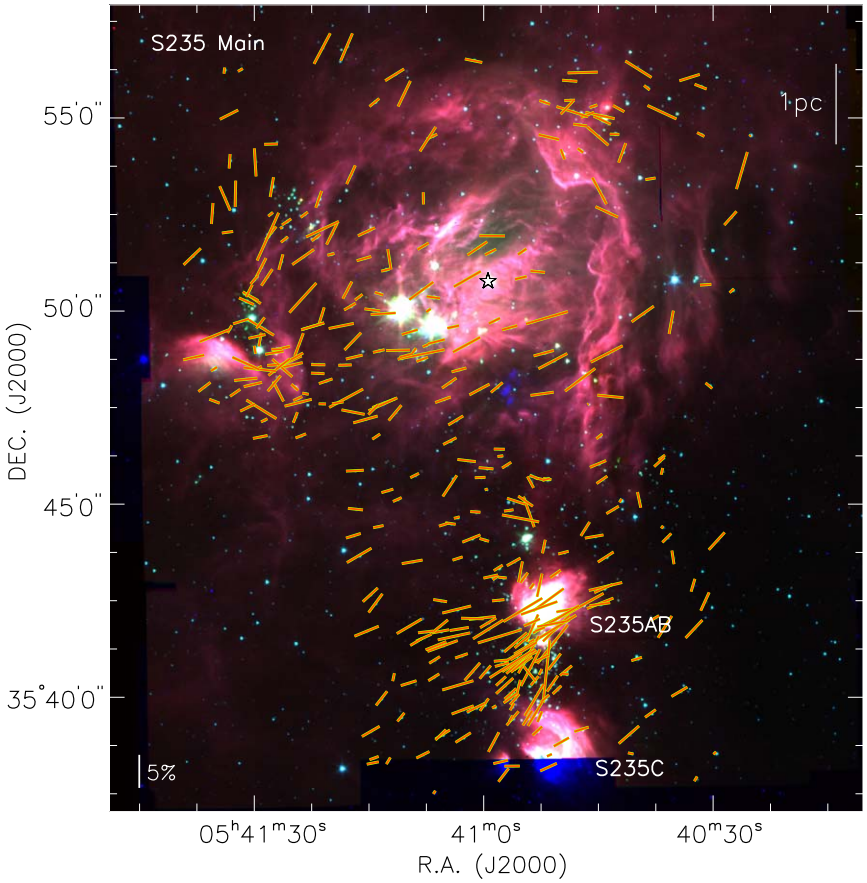

Figure 8. Magnetic field morphology in the S235 complex. The background image is the same Spitzer IRAC three-color-composite map shown in Figure 1. The NIR background starlight polarizations are indicated by red–yellow pseudo-vectors. The lengths of the vectors indicate the polarization percentages, and a reference vector length is shown at the bottom left. The PAs of these vectors trace the POS magnetic field orientations in the S235 complex.

(Heitsch et al. 2001; Ostriker et al. 2001) have shown that the Q value may be approximated as 0.5, yielding reliable results for $B_{\rm pos}$, provided that the PA dispersion is less than 25°. Adopting $Q = 0.5$, Equation (9) reduces to

$$B_{\rm pos} = 1.77\left(\frac{\sqrt{\rho}}{1\ {\rm gm\ cm^{-3}}}\right)\left(\frac{\sigma_v}{1\ {\rm cm\ s^{-1}}}\right)\left(\frac{1\ {\rm rad}}{\delta\theta}\right)(\mu{\rm G}). \quad (10)$$

We estimated $\delta\theta$ values from the background starlight polarization angles. Each dispersion value was calculated by taking the variance-weighted standard deviation of all of the PA values within each clump boundary. Since the PA values have 180° ambiguity, de-aliasing was necessary (Hoq et al. 2017; Wang et al. 2020). This was carried out by stepping the aliasing window through increments of 1° between 0° and 180°. The minimum standard deviation from all of the de-aliased sets was chosen as the final dispersion value for each clump.

The σ_v values were obtained from the ^{13}CO spectra associated with each clump. The spectrum at each pixel was fit by a Gaussian to obtain the standard deviation, i.e., the dispersion value. The mean velocity dispersion for each clump was computed as the weighted average of all standard deviation values within the clump boundary. Although velocity dispersion is based on observed properties along the LOS, it is considered to be a valid value for the POS under the assumption that the turbulent motions are isotropic (e.g., Hoq et al. 2017).

The mass volume density ρ, was determined from the average column density values. The volume number density was estimated as $n_{\rm H_2} = N({\rm H_2})^{\rm avg}_{1.1} \Big/ \frac{4}{3}R_{\rm eff}$ based on the assumption of a uniform density spherical clump. For the diffuse regions, $n_{\rm H_2}$ was estimated as $N({\rm H_2})^{\rm avg}_{\rm CO}/ln$, where ln is the cloud depth along the LOS. Depths of filamentary clouds can be characterized by assuming a cylindrical morphology with determination of their spine axis and inclination, but the S235 cloud is distributed inhomogenously around the shell of the H II region. Hence, we chose ln to be an intermediate value greater than the clump sizes (∼1 pc) but smaller than the diameter of the H II region shell (∼3 pc). Based on this, an empirical mean of $ln = 2$ pc was taken for the diffuse regions. The mass volume density was finally calculated as $\rho = n_{\rm H_2}(\mu_{\rm H_2})(m_{\rm H})$, where $\mu_{\rm H_2}$ and $m_{\rm H}$ are the same as defined earlier.

The magnetic field strength for the 11 clumps and the two diffuse regions was estimated using the DCF-method (see Table 5). The uncertainties were estimated by propagating the uncertainties of the PA dispersions, the velocity dispersions, and the volume densities.

A map of clump-averaged $B_{\rm pos}$ is shown in Figure 11, with a color bar indicating the mapping of color to magnetic field strength. The clumps have values ranging from 36 to 121 μG, with a mean value of ∼65 μG. The $B_{\rm pos}$ for clump 11 is less reliable since its $\delta\theta$ exceeds 25°. Clumps in the central region

Table 3
Polarimetric and Photometric Properties of the 375 Foreground-corrected Embedded and Background Stars in the S235 Complex

ID	R.A. (J2000)	Decl. (J2000)	P' (%)	PA (deg)	Q (%)	U (%)	J[a] (mag)	H (mag)	K (mag)	A_V (mag)	Distance[b] (kpc)
1	85.10488	35.90900	0.3 (0.2)	129 (12)	−0.1 (0.1)	−0.3 (0.2)	13.22 (0.02)	11.85 (0.02)	11.25 (0.02)	7.1 (0.5)	$1.9\vert^{3.2}_{1.3}$
2	85.10932	35.89397	5.9 (2.3)	159 (10)	4.8 (2.3)	−4.1 (2.2)	16.38 (0.09)	15.34 (0.08)	14.74 (0.09)	7.2 (1.9)	$2.1\vert^{4.2}_{0.9}$
3	85.11484	35.84210	1.0 (0.2)	124 (5)	−0.4 (0.2)	−0.9 (0.2)	13.67 (0.02)	12.25 (0.02)	11.64 (0.02)	7.2 (0.5)	$3.0\vert^{5.0}_{1.9}$
4	85.11559	35.87341	3.1 (2.4)	131 (21)	−0.4 (2.3)	−3.9 (2.4)	16.10 (0.11)	14.90 (0.07)	14.12 (0.09)	9.9 (1.2)	⋯
5	85.12303	35.73406	4.0 (2.0)	130 (14)	−0.6 (2.0)	−4.4 (2.0)	16.32 (0.19)	15.05 (0.08)	14.36 (0.08)	8.6 (1.4)	⋯
6	85.12410	35.64257	0.6 (0.6)	125 (26)	−0.3 (0.6)	−0.8 (0.6)	13.89 (0.02)	12.28 (0.02)	11.66 (0.02)	7.3 (0.4)	$2.0\vert^{4.0}_{1.2}$
7	85.12731	35.80114	1.5 (0.4)	56 (9)	−0.6 (0.4)	1.4 (0.4)	14.59 (0.03)	13.03 (0.02)	12.31 (0.02)	9.0 (0.5)	$2.2\vert^{4.3}_{1.1}$
8	85.12906	35.84469	2.2 (1.5)	93 (22)	−2.6 (1.5)	−0.3 (0.5)	15.55 (0.05)	14.26 (0.04)	13.86 (0.04)	3.9 (0.9)	$1.6\vert^{3.7}_{0.7}$

Notes. Only a portion of this table is shown here to demonstrate its form and content. A machine-readable version of the full table is available. Missing data are shown here as ellipses but are represented by the number 0.0 in the machine-readable version. Uncertainties are given in parentheses.
[a] J, H, and K band magnitudes from 2MASS or UKIDSS data.
[b] Distance values from Bailer-Jones et al. (2018) catalog with their low and high uncertainties.

(This table is available in its entirety in machine-readable form.)

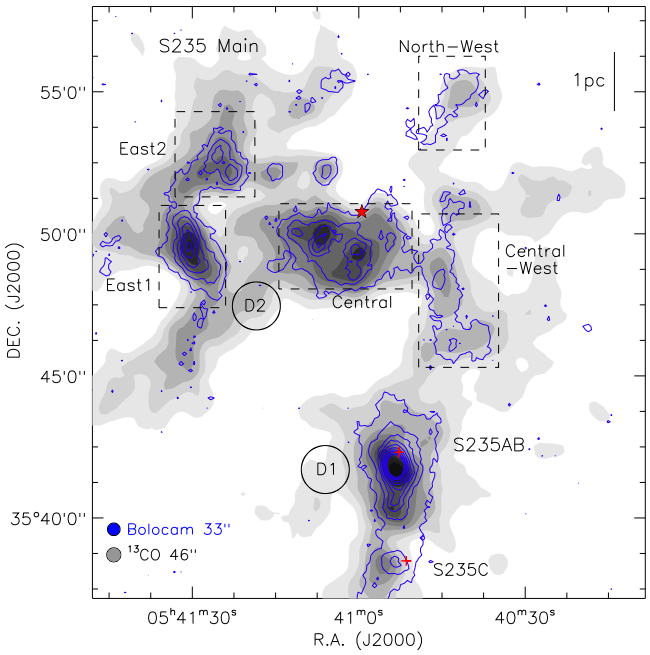

Figure 9. The distribution of molecular gas and dust emission in the S235 complex. The ^{13}CO integrated intensity (Brunt 2004) between $V_{\rm LSR}$ − 25 to − 15 km s^{-1} is shown by the filled gray contours. The contour levels range from 10% to 90% of the peak value of 37.3 K km s^{-1}. The Bolocam 1.1 mm (Ginsburg et al. 2013) dust continuum intensity emission is overlaid as blue contours, ranging from 5% to 95% of the peak value of 2.0 Jy/beam. Subregions identified by Kirsanova et al. (2008) are shown by dashed boxes. Two diffuse regions, D1 and D2, used for magnetic field estimates of the cloud are shown as circles. The ellipses in the lower left corner represent the angular resolutions of the Bolocam (33″) and ^{13}CO (46″) data.

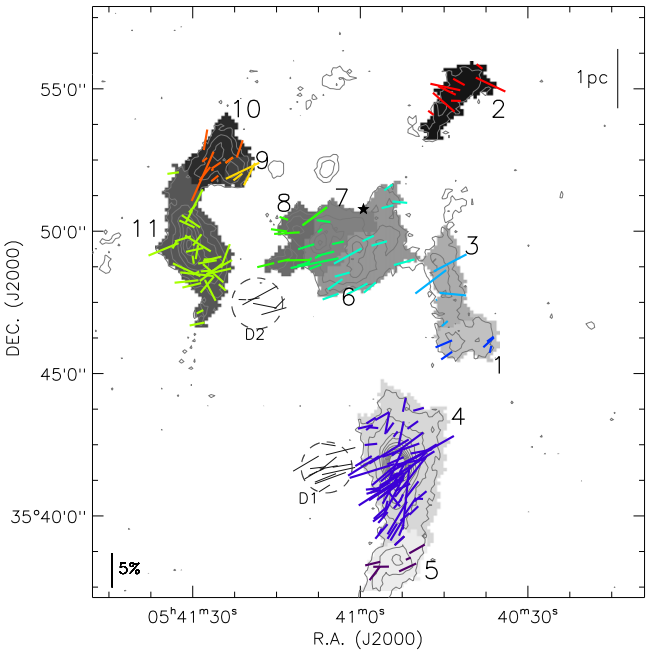

Figure 10. The dense clumps identified in the Bolocam 1.1 mm dust emission are shown as zones of different gray shades. The contours and boundaries are the same as in Figure 9. The NIR embedded and background starlight polarization vectors are overplotted in different colors to show the magnetic field orientations in each clump. The diffuse regions in the cloud, D1 and D2, are shown as dashed circles, also with their polarization vectors.

have relatively higher $B_{\rm pos}$ values due to their lower polarization PA dispersions. The diffuse regions D1 and D2 have smaller values and average about 34 μG. Overall, these 13 values are similar to the typical values for magnetic field strengths in Galactic molecular clouds, which range from 1 to 100 μG for volume densities 10^3–10^4 cm^{-3}, obtained from Zeeman observations (Bourke et al. 2001; Troland & Crutcher 2008) and polarized dust emission (Crutcher et al. 2004; Li et al. 2018).

We note that the magnetic field strength estimates can be dominated by large errors despite the use of the most reliable observational parameters. These values are influenced by systematic uncertainties such as distance, inclination angle, flux calibration, dust temperature, and clump geometry (Crutcher et al. 2004; Li et al. 2018). Some of these systematic uncertainties may be minimal in the S235 analyses. For example the distance has been precisely determined using the Gaia DR2 parallax of the ionizing star. The main contribution of the systematic uncertainty is from the assumption of uniform density spherical clumps with a uniform dust temperature ($T_d = 20$ K). Therefore, the real uncertainties of the magnetic field strength estimates could be larger than the quoted values.

Table 4
Properties of Bolocam 1.1 mm Dust Clumps

Clump ID	R.A. (J2000)	Decl. (J2000)	$R_{\rm eff}$ (pc)	S_ν (Jy)	$M_{\rm iso}$ ($M_\odot$)	$M_{\rm vir}$ ($M_\odot$)	$N(H_2)^{\rm avg}_{1.1}$ (10^{21} cm^{-2})	$N(H_2)^{\rm int}_{1.1}$ (10^{22} cm^{-2})
1	85.17199	35.76990	0.40	1.49 (0.29)	53 (12)	416 (71)	4.74 (1.13)	3.01 (1.20)
2	85.17990	35.91203	0.48	1.25 (0.35)	44 (13)	360 (126)	2.68 (0.83)	2.52 (1.41)
3	85.18770	35.80451	0.42	2.02 (0.52)	72 (20)	362 (103)	5.61 (1.62)	4.08 (2.1)
4	85.22087	35.69645	0.75	14.77 (0.49)	525 (72)	1080 (152)	13.19 (1.81)	29.75 (1.97)
5	85.22495	35.63886	0.43	2.45 (0.36)	87 (17)	467 (102)	6.70 (1.34)	4.93 (1.47)
6	85.24700	35.82111	0.68	5.25 (0.67)	186 (34)	1891 (497)	5.59 (1.03)	10.57 (2.7)
7	85.27268	35.82915	0.51	4.36 (0.43)	155 (25)	1204 (273)	8.35 (1.38)	8.78 (1.73)
8	85.29919	35.83027	0.35	1.40 (0.34)	49 (14)	426 (110)	5.62 (1.57)	2.82 (1.39)
9	85.34428	35.86830	0.26	0.94 (0.18)	33 (8)	184 (40)	7.05 (1.63)	1.91 (0.72)
10	85.35845	35.87669	0.37	2.19 (0.30)	77 (15)	336 (50)	7.93 (1.53)	4.41 (1.23)
11	85.37528	35.82512	0.64	6.76 (0.42)	240 (35)	502 (57)	8.27 (1.21)	13.63 (1.69)

Note. Uncertainties are given in parentheses.

4.5. Magnetic Energy versus Gravitational, Turbulent, and Thermal Energies

4.5.1. Mass-to-flux Ratio

The importance of the magnetic field with respect to gravity can be probed by considering the ratio of the mass of an object to its magnetic-critical mass $M_{\Phi,\rm crit}$. The magnetic-critical mass is defined by the condition that magnetic energy is equal to the gravitational energy for a region in magnetostatic equilibrium and is given as (Mouschovias & Spitzer 1976; McKee & Ostriker 2007):

$$M_{\Phi,\rm crit} = \frac{\Phi}{2\pi\sqrt{G}}, \tag{11}$$

where $\Phi = B_{\rm tot}\pi R_{\rm eff}^2$ is the magnetic flux threading a region of a given radius.

Crutcher et al. (2004) presented these parameters into a dimensionless quantity called the normalized mass-to-flux ratio ($\overline{M/\Phi_B}$). This can be calculated from the magnetic field strength as:

$$\overline{M/\Phi_B} = \frac{M_{\rm iso}}{M_{\Phi,\rm crit}} = 7.6\times10^{-21}\frac{N(H_2)}{B_{\rm tot}}, \tag{12}$$

where $N(H_2)$ is the average column density (in cm^{-2}), and $B_{\rm tot}$ is the three-dimensional total magnetic field strength (in microgauss). Since linear polarization observations provide only $B_{\rm pos}$, the LOS component needed to form the $B_{\rm tot}$ is missing. Crutcher et al. (2004) showed that the total magnetic strength can be estimated as $B_{\rm tot} = 1.3B_{\rm pos}$, based on statistical analysis for an average field geometry and projection effects. We applied this for the $B_{\rm tot}$ estimates.

Determining $\overline{M/\Phi_B}$ allows one to assess the stability of a region. If $\overline{M/\Phi_B} > 1$, the region is supercritical and gravitationally unstable, whereas when $\overline{M/\Phi_B} < 1$, it is subcritical and supported by magnetic fields.

Based on the values of $N(H_2)^{\rm avg}$ and $B_{\rm pos}$, we estimated the mass-to-flux ratios for the clumps and the diffuse regions (see Table 5). The $\overline{M/\Phi_B}$ values range between 0.3 and 1.3 with a median of about 0.6. These values correspond to subcritical states of the clumps, implying a dominant role of the magnetic field. The diffuse regions have values of 0.4 and 0.6, suggesting that the magnetic field also dominates in the diffuse parts of the cloud.

4.5.2. Turbulent Alfvénic Mach Number and Plasma Beta

The relative importance of gas turbulence with respect to the magnetic field can be described by the turbulent Alfvén Mach number $\mathcal{M}_{\rm A}$, and is an important factor in determining the evolution of clumps.

The Alfvénic Mach number can be estimated as:

$$\mathcal{M}_{\rm A} = \frac{\sigma_{\rm NT}}{\mathcal{V}_{\rm A}}, \tag{13}$$

where the Alfvén speed is given by $\mathcal{V}_{\rm A} = B_{\rm tot}/\sqrt{4\pi\rho}$, and $\sigma_{\rm NT}$ is the nonthermal gas velocity dispersion. The nonthermal velocity dispersion was estimated as $\sigma_{\rm NT} = \sqrt{\sigma_v^2 - \sigma_{\rm T}^2}$, where $\sigma_{\rm T}$ is the thermal line broadening, taken to be 0.15 km s^{-1}, using values obtained from NH_3 line observations (Kirsanova et al. 2014; Dewangan et al. 2016).

Models by Padoan et al. (2001) and Nakamura & Li (2008) suggest that sub-Alfvénic ($\mathcal{M}_{\rm A}\leqslant 1$) magnetic fields are strong enough to regulate gas motions and allow gas to move along the field lines to form high-density structures. In the super-Alfvénic case ($\mathcal{M}_{\rm A}> 1$), gas turbulence can efficiently change the magnetic field from ordered to a more random morphology.

The turbulent plasma beta parameter β_p characterizes the importance of magnetic fields with respect to the thermal energy within a clump. It is defined as the ratio of thermal to magnetic pressure:

$$\beta_p = \frac{P_{\rm therm}}{P_{\rm mag}} = \frac{2c_s^2}{\mathcal{V}_{\rm A}^2}, \tag{14}$$

where c_s is the sound speed in the neutral medium, calculated as $c_s = \sqrt{\frac{kT_g}{\mu_{H_2} m_{\rm H}}} = 0.24$ km s^{-1}, for an average gas temperature of $T_g = 20$ K (Kirsanova et al. 2014).

The estimated values of $\mathcal{M}_{\rm A}$ and β_p are listed in Table 5. The clumps show values consistently below unity for both parameters, indicating sub-Alfvénic conditions, and implying a strong magnetic field with respect to both turbulence and thermal pressure.

Table 5
Magnetic Field Properties in the S235 Complex

Clump ID	No. of Stars	$\delta\theta$ (degree)	σ_v (km s^{-1})	n_{H_2} (cm^{-3})	B_{pos} (μG)	$\overline{M/\Phi_B}$	$\mathcal{M}_A$	β_p ($\times 10^{-2}$)
1	5	21.3 (2.6)	0.91 (0.06)	2890 (690)	50 (9)	0.5 (0.2)	0.6 (0.1)	4.5 (1.6)
2	8	11.0 (1.7)	0.55 (0.04)	1350 (420)	40 (9)	0.4 (0.2)	0.3 (0.1)	3.2 (1.4)
3	5	15.4 (2.2)	0.71 (0.08)	3190 (920)	57 (14)	0.6 (0.2)	0.4 (0.1)	3.8 (1.8)
4	69	17.2 (1.7)	0.99 (0.05)	4270 (590)	82 (11)	0.9 (0.2)	0.5 (0.1)	2.5 (0.5)
5	7	15.2 (2.3)	0.81 (0.05)	3790 (760)	72 (13)	0.5 (0.2)	0.4 (0.1)	2.9 (1.0)
6	12	10.4 (1.4)	1.03 (0.05)	1980 (370)	97 (16)	0.3 (0.1)	0.3 (0.1)	0.8 (0.3)
7	11	11.7 (1.5)	1.02 (0.05)	3960 (660)	121 (19)	0.4 (0.1)	0.3 (0.1)	1.1 (0.3)
8	7	14.3 (2.1)	0.82 (0.03)	3860 (1080)	78 (16)	0.4 (0.2)	0.4 (0.1)	2.5 (1.0)
9	4	15.8 (2.4)	0.66 (0.02)	6580 (1520)	74 (14)	0.6 (0.2)	0.4 (0.1)	4.7 (1.6)
10	9	19.7 (2.7)	0.82 (0.02)	5170 (990)	66 (11)	0.7 (0.2)	0.5 (0.1)	4.8 (1.4)
11[a]	33	29.0 (5.7)	0.85 (0.04)	3130 (460)	36 (8)	1.3 (0.4)	0.8 (0.2)	9.5 (3.2)
D1	13	10.8 (1.5)	0.77 (0.09)	370 (110)	30 (7)	0.4 (0.2)	0.3 (0.1)	1.6 (0.7)
D2	6	17.1 (2.6)	1.21 (0.09)	630 (200)	39 (9)	0.6 (0.3)	0.5 (0.2)	1.7 (0.8)

Notes. Uncertainties are given in parentheses.
[a] Clump 11 has $\delta\theta$ greater than 25°, and hence its magnetic field estimates are less reliable.

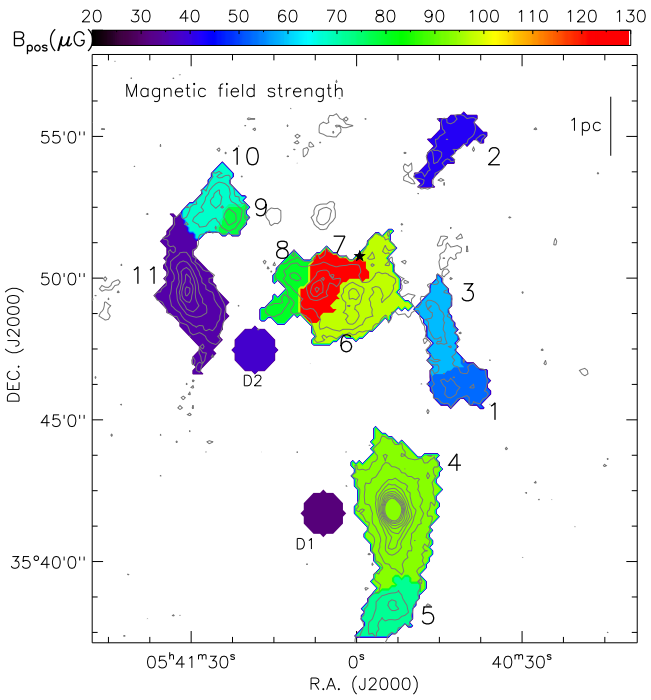

Figure 11. Map of clump-averaged B_{pos} for the S235 complex, estimated using the DCF-method. The identified clumps and two diffuse regions of the cloud (D1 and D2) are highlighted in different colors corresponding to their average B_{pos} strengths. The color bar at the top indicates the range of B_{pos} values.

4.5.3. Virial Analysis

A virial analysis was performed to check if the clumps are currently in gravitational equilibrium. The virial mass, considering thermal, turbulent, and magnetic energies, is given as (Pillai et al. 2011; Li et al. 2018):

$$M_{vir} = 3\frac{R_{eff}}{G}\left(\frac{5-2i}{3-i}\right)\left(\sigma_{NT}^2 + c_s^2 + \frac{\mathcal{V}_A^2}{6}\right) \quad (15)$$

where i is the spectral index for the density profile $\rho(r)$ as a function of the distance (r) from the clump center, $\rho(r) = r^{-i}$. We adopt $i = 1.8$ from the Mueller et al. (2002) analysis of 31 massive star-forming clumps in other Galactic regions. The σ_{NT}, c_s, and $\mathcal{V}_A$ terms are the same as defined previously. The resulting virial masses for the clumps are listed in Table 4. The clumps show consistently larger virial masses than their isothermal masses, indicating that the regions are gravitationally stable against collapse. Therefore, the likelihood of formation of new stellar clusters in the S235 complex is currently low.

5. Discussion

The analyses of 375 embedded and background starlight polarizations revealed the POS magnetic field orientations in the S235 complex. Estimates of clump magnetic field properties showed that the magnetic fields are dynamically important with respect to gravitational and turbulent energies. In this section, we discuss the properties of dust grain alignment, the distribution of magnetic field orientations around the H II region, and the role of magnetic fields in triggered star formation.

5.1. Polarization Efficiency

Properties of dust grain alignment with respect to the local magnetic field may be revealed through the polarization efficiency. It is defined as the ratio of the polarization percentage to the extinction (PE $= P_\lambda/A_V$). The grain alignment model of radiative torque alignment (RAT; Lazarian & Hoang 2007; Hoang & Lazarian 2008) requires that anisotropic radiation imparts a net torque on the asymmetric dust grains. The dust grains then precess and align their rotational axes with the local magnetic field. A main prediction of RAT theory is that PE should decreases with increasing in A_V, since the radiation required to align the dust gets absorbed prior to reaching the denser regions.

We compared the H-band polarization percentage versus extinction for the embedded and background stars, and the results are shown in Figure 12(A). The polarization values exhibit an increasing trend with extinction, especially for $A_V > 3$ mag, reaching a maximum polarization of about 8%–10% for

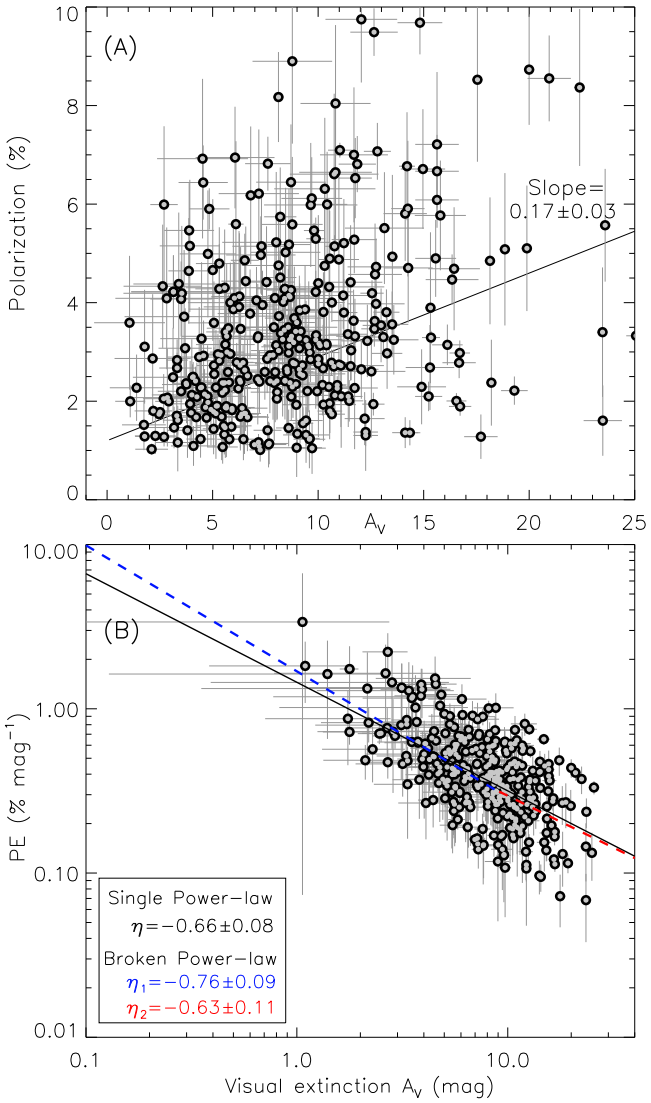

Figure 12. Panel (A): plot of polarization percentage vs. extinction for the 375 embedded and background stars in the S235 complex. A variance-weighted least-squares fit gives a slope of 0.17 ± 0.03. Panel (B): log–log plot of polarization efficiency vs. extinction for the same stars in panel (A). A single variance-weighted power-law fit on the values is shown by the black solid line, which has an index of $\eta = -0.66 \pm 0.08$. A broken power-law fit is shown by the dashed blue and red lines, respectively. They have indices $\eta_1 = -0.76 \pm 0.09$ and $\eta_2 = -0.63 \pm 0.11$, respectively.

$A_V \sim 15$ mag. The P versus A_V relation was fit with a variance-weighted least-squares line, giving a slope of 0.17 ± 0.03. The positive slope is close to the value of 0.2 obtained by Kusune et al. (2015) for dense clouds at the peripheries of other H II regions. Other studies have shown a lower P versus A_V slope of about 0.1 (Arce et al. 1998; Hoq et al. 2017) with predictions of decrease in polarization efficiency at large opacities in their clouds. The slope of 0.17 ± 0.03 found for the S235 complex may be attributed to typical dust grains (0.1–0.5 μ m) that remain efficiently aligned by radiation to substantial optical depths (see review by Andersson et al. 2015).

The relation between PE and A_V has been characterized for other clouds using a power-law behavior ($PE \propto A_V^{\eta}$) mostly to match predictions of RAT theory. Several studies have shown that the power-law indices range from $\eta = -0.3$ to -0.7 (Whittet et al. 2008; Chapman et al. 2011; Alves et al. 2014; Cashman & Clemens 2014) for medium- to high-opacity clouds. Figure 12(B) compares the PE versus A_V for embedded and background stars in the S235 complex. We fit a single variance-weighted power law to the values and obtained a slope of $\eta = -0.66 \pm 0.08$. The PE tends to be greater for stars with low extinctions, up to $A_V \sim 5$ mag, and becomes lesser for higher extinctions. This might indicate that the high PE values are associated with grains lying in the envelopes of the clumps.

Whittet et al. (2008) used a large sample of K-band polarimetry toward Taurus and Ophiuchus clouds to find a single power-law index of -0.52 ± 0.07 over the full range of $A_V = 0 - 30$ mag. However, their predictions of RAT modeling suggested that a break point should exist at higher extinctions. Alves et al. (2014) showed that the PE in Pipe nebula exhibits a break point at $A_V \sim 10$ mag, interpreted as being due to a mixed distribution of grain sizes from cloud to dense cores. Wang et al. (2017) performed a similar study with the IC5146 cloud and found that the PE in the H band drops steeply ($\eta = -0.95 \pm 0.30$) up to $A_V \sim 3$ mag, but then changes to a softer value ($\eta = -0.25 \pm 0.10$) for greater A_V.

To test whether the PE versus A_V relation has a break point for the S235 complex, we fit a broken power law of the form:

$$PE = \begin{cases} \alpha_1 A_V^{\eta_1} & : A_V \leqslant x_{\rm break} \\ \alpha_2 A_V^{\eta_2} & : A_V > x_{\rm break}, \end{cases} \tag{16}$$

where $\alpha_2 = \alpha_1 x_{\rm break}^{\eta_1 - \eta_2}$. The parameters, α_1, η_1, η_2, and x_{break}, were taken as free parameters for the broken power-law fit.

We find the slopes of the broken power law to be $\eta_1 = -0.76 \pm 0.09$ and $\eta_2 = -0.63 \pm 0.11$. These are represented by the dashed blue and red lines in Figure 12(B). The difference in the slopes for the broken power-law case and the single power-law case is small. This indicates that the PE versus A_V behavior likely changes systematically over the entire A_V range in the S235 complex. This general decrease in PE within the cloud may arise if the grain size distribution are the same in the diffuse and denser regions. This requires no significant grain growth, which if present would be expected to display a flatter index at large A_V.

A possible caveat in the η estimates arises from the uncertainty in the A_V calculations. This is due to the estimation of A_V by assumption of intrinsic stellar colors without knowing their spectral types. However, this should not significantly change the PE versus A_V trend. Hence, we assume the background star polarization is tracing the magnetic field within the clumps as predicted by RAT theory.

5.2. Magnetic Field Distribution

5.2.1. Large-scale Magnetic Field

The global polarization orientations shown in Figure 8 reveal an ordered magnetic field throughout the S235 cloud. Studies have suggested that molecular clouds tend to preserve large-scale magnetic field orientations (see Li et al. 2014; Clemens et al. 2018) for which gravitational flow of gas is unconstrained along the magnetic field lines. We used the Planck polarized dust emission, rotated 90° to reveal the large-scale field structure. Figure 13 shows a magnetic field map using NIR and Planck data. Both data sets exhibit similar large-scale patterns, with their magnetic field orientations being mostly parallel to the Galactic plane. Several polarization surveys show similar distributions, where polarization angles tend to present an overall plane-parallel orientation (Mathewson & Ford 1970;

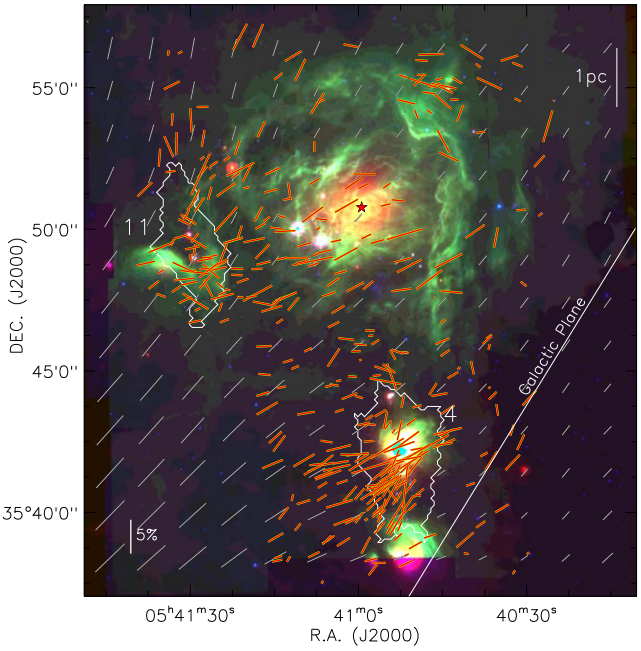

Figure 13. Large-scale magnetic field orientations in the S235 complex. The background image is a three-color composite map using Spitzer MIPS and IRAC bands: 24 μm (red), 8 μm (green), and 3.6 μm (blue). The Planck polarizations, rotated 90°, tracing the large-scale magnetic field, are shown as gray vectors. The NIR polarization is shown as red–yellow vectors. The direction of the Galactic plane is shown as a solid white line. Clumps 4 and 11 used in comparing the NIR and Planck polarizations are highlighted by their boundaries.

Heiles & Crutcher 2005; Clemens et al. 2012a). The S235 complex is situated in the Milky Way Perseus spiral arm and extends to a latitude of $b \approx +2.^{\circ}8$. At these latitudes, the bulk of the gas still remains a part of the spiral arms, and the large-scale magnetic fields are believed to have their origin due to differential rotation in the Galactic disk (Beck et al. 1996; Beck 2015).

We quantitatively compared the magnetic field orientations from the NIR and Planck data sets. The mean polarization angle in the NIR data is $114° \pm 4°$ and for the Planck data (rotated 90°) is $121° \pm 2°$. The difference between the data sets is small, indicating that polarization due to dust absorption and dust emission are tracing the same component of the magnetic field at larger scales. At smaller scales, the NIR and Planck data differ. We compared the polarization angles for clumps 4 and 11, which have sizes similar to the Planck effective beam size of 5′ (~2 pc). Other clumps were excluded, as their sizes are smaller than the Planck beam. Clump 4 shows a strikingly similar value between NIR ($123° \pm 3°$) and Planck ($122° \pm 1°$), whereas clump 11 has a significant difference, with values $110° \pm 4°$ and $148° \pm 2°$, respectively. This discrepancy in the results could be due to turbulence from stellar feedback significantly altering the small-scale magnetic field orientations. Hence, Planck polarization is useful for mainly sampling the large-scale ordered magnetic fields.

5.2.2. Magnetic Field in the Shell

The most prominent result seen in the *H*-band polarization observations is the curved magnetic field morphology around the S235 Main region (see Figures 8 and 13). This pattern coincides with the location and morphology of the mid-infrared PDR shell that encompasses the expanding H II region. The shell is created when the expanding H II region pushes the surrounding material via radiation and thermal pressure. As the ionization front expands, it causes inhomogeneities and changes in the density of the material. Hence, the gas around the shell gets compressed and is seen tracing a shell-like morphology in Figure 9. Since the magnetic field is coupled to the gas, the field lines are dragged in this process, causing them to follow the spherical pattern of the shell.

Several numerical simulations incorporating magnetic fields (Krumholz et al. 2007; Arthur et al. 2011) have shown curvature in magnetic field orientations due to expansions of H II regions. This has also been revealed in observational studies (e.g., Santos et al. 2014; Chen et al. 2017; Dewangan et al. 2018), where magnetic fields are found to be aligned tangentially to H II region shells. The curvature of field lines in S235 Main is mainly at the edges of the shell and corresponds to distance of about 2.4 pc from the ionizing star. A typical bubble/shell-like H II region consists of an inner ionized region surrounded by a PDR envelope with a thickness of about 0.2–0.4 pc (Churchwell et al. 2006). Hence, the magnetic field distribution is mainly affected at the outer layers, where the ionization front interacts with the ambient molecular gas.

Recent studies on the structure of the S235 Main H II region using ionized and molecular emission suggest that the molecular material in the LOS is mainly distributed in the rear and side walls of the PDR shell (see Figure 8 of Anderson et al. 2019; Kirsanova et al. 2020). This indicates that the magnetic field directions traced in clumps 6, 7, and 8 are associated with the regions behind the ionizing star.

Arthur et al. (2011) showed with simulations that the H II region expands largely parallel to the ambient magnetic field, and over-dense regions are created at the edges of the elongated end caps. The magnetic field lines in S235 Main show a similar distribution with slight elongation parallel to the large-scale Galactic magnetic field. Additionally, the northwest and southeast regions are associated with dense molecular material (clumps 2 and 11), which appears to be projected at the outer edge of the H II region. This observational feature correlates well with the simulations and supports the prediction that the ionization front compresses the surrounding neutral gas into denser regions. These dense regions have been observed to harbor a number of YSOs (Kirsanova et al. 2014; Dewangan et al. 2016). Hence, the formation of these YSOs is attributed to the effect of the expanding H II region.

5.3. The Role of Magnetic Fields in Triggered Star Formation

Triggered star formation has normally been considered in the context of weak magnetic field models (Crutcher 2012), where supersonic turbulent flows dominate the evolution of molecular clouds. On the other hand, strong magnetic field models (Mouschovias 1991; Mouschovias & Ciolek 1999) suggest that molecular clouds are supported by well-ordered magnetic fields through their outward pressure, which later quasi-statically dissipate via ambipolar diffusion (Mestel & Spitzer 1956). Eventually on core scales, self-gravity overcomes magnetic forces, inducing collapse and the formation of stars (Mouschovias et al. 2006).

The S235 complex has been studied extensively to seek evidence for triggered star formation (Dewangan & Anandarao 2011; Kirsanova et al. 2014; Dewangan et al. 2016; Dewangan & Ojha 2017). These studies have found large numbers of YSO clusters in the molecular gas. The studies have comprehensively arrived to the conclusion that YSO

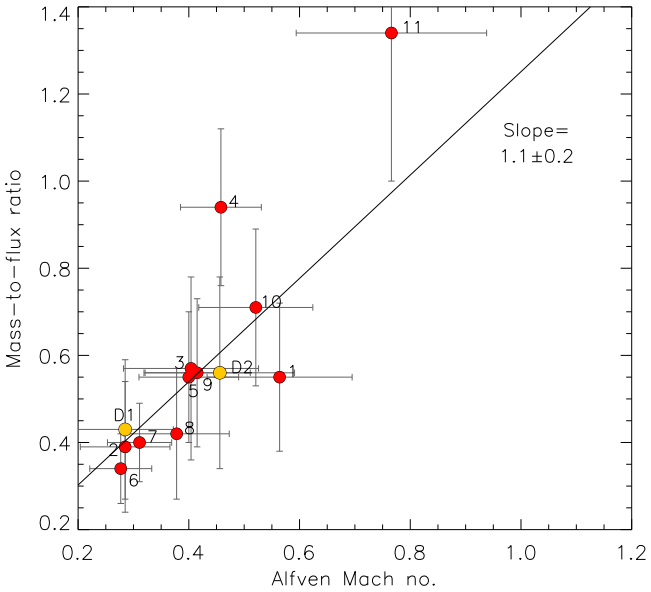

Figure 14. Plot of normalized mass-to-flux ratio vs. Alfvén Mach number for the clumps (red points) and diffuse regions (yellow points) of the S235 complex. The clump numbers are highlighted next to each data point. There is a tight linear dependence of both quantities, except for clump 11, which has less reliable values due to its large polarization PA dispersion (see Section 4.4). A variance-weighted least-squares fit gives a slope of 1.1 ± 0.2.

clusters are the result of positive stellar feedback driven by the expansion of the S235 Main H II region. The S235AB and S235C regions have also been observed to contain a number of YSOs. Felli et al. (2006) proposed that these clusters could have formed due to the expanding H II region from massive star in S235A. However, other studies indicate that the region associated with S235A is a young ultra-compact H II region of about 0.2 Myr (Dewangan & Anandarao 2011) and lacks the energetics to trigger new stars in the surrounding molecular core (Kirsanova et al. 2014). Hence, we focus our discussion of magnetic fields and triggered star formation mainly on the S235 Main region.

Several observational studies find molecular clouds to be magnetically supercritical (Crutcher 1999, 2012). In contrast, the S235 complex is magnetically subcritical. The three parameters for criticality: $\overline{M/\Phi_B}$, $\mathcal{M}_{\rm A}$, and β, estimated from our observations, show values less than unity. The individual clumps show subcritical states and are not in virial equilibrium. The Alfvén Mach number values suggest that the clumps are sub-Alfvénic, and hence the role for turbulence is minimal. These results indicate that strongly magnetized conditions prevail, both in the dense clumps and diffuse regions of the S235 complex. We compared the values of the mass-to-flux ratio to the Alfvén Mach number for the clumps and diffuse regions, as shown in Figure 14. There is a tight linear correlation between both quantities, where $\overline{M/\Phi_B}$ increases for increasing $\mathcal{M}_{\rm A}$. A variance-weighted least-squares fit returns a slope of 1.1 ± 0.2. The positive linear slope indicates that the magnetic fields dominate equally against both gravity and turbulence.

In order to understand how triggered star formation proceeds in S235 Main in the presence of strong magnetic fields, we consider the evolution, fragmentation, and diffusion timescales of the complex. Before the expansion of the S235 Main H II region, the strong magnetic fields in the parental cloud likely helped keep the region in gravitational equilibrium. As the H II region expanded, it created over-dense regions, since supersonic turbulence from the shock fronts compressed the molecular gas. The magnetic fields at this stage did not provide sufficient pressure to counter the ionization fronts. This period lasted a short amount of time, for about 0.1 Myr (Elmegreen & Lada 1977), after which it led to core collapse, forming low-mass stars or even high-mass stars, as predicted by competitive accretion (Tan et al. 2014). The turbulence driven by the shock fronts decayed rapidly, with the regions transitioning into sub-Alfvénic states. The magnetic fields in the envelopes still preserved their subcritical natures. This describes the current conditions present in the S235 Main region.

Bisbas et al. (2011) carried out numerical simulations of triggered star formation, where preexisting dense condensations were compressed by the pressure of the ionized gas. Their results showed that star formation mainly occurs during the initial phases of the interactions of shock fronts with quiescent ambient molecular gas, when the ionizing photon fluxes are high (of the order of 10^9–10^{11} cm^{-2} s^{-1}). They also demonstrated that the sequence of triggered star formation occurs on a rapid timescale, about 0.19 Myr. Mackey & Lim (2011) showed that the energy from photoionization at the boundaries of an H II region is significantly stronger than the magnetic fields present there. Hence, turbulence is the dominant driver at the initial stages that leads to gas compression in the forms of pillars and globules. Arthur et al. (2011) studied the evolution of an H II region in a turbulent, magnetized molecular cloud and found that after the expansion of the H II region, the magnetic fields in the shell are amplified and slow the formation of new stars.

These modeling results, considered in the context of our new observations, can be interpreted as follows. The first generation of triggered stars in the S235 Main formed rapidly from the effects of expansion of the H II region. The formation of subsequent generations of stars from the remaining dense gas and envelope has been slowed by the strong magnetic fields present, as revealed in our observational results. Hence, turbulence from stellar feedback plays a positive role during the initial stages of triggered star formation, followed by magnetic fields regulating the star formation process thereafter.

5.3.1. Magnetic Field versus Density

The relation between magnetic field strength and gas density ($B_{\rm tot} \propto n_{\rm H}^{\kappa}$) can be used to predict the role of magnetic fields in the formation of new clumps. If magnetic fields are important, dense regions must form primarily from flows of weakly ionized, but mostly neutral, gas along the field lines. Fiedler & Mouschovias (1993) carried out detailed numerical simulations of strong field models with ambipolar diffusion-driven cloud contraction and obtained $\kappa \approx 0.47$. Crutcher (1999) used Zeeman observations of 27 clouds and obtained $\kappa = 0.47$ for a wide range of densities from 10^3 to 10^6 cm^{-3}, thus favoring the predictions of ambipolar diffusion-driven star formation. Conversely, Crutcher et al. (2010) employed Bayesian statistical analysis of observational data for a wide variety of individual cloud observations, including upper limits, and found $\kappa = 0.65$ for gas number densities greater than 300 cm^{-3}. They suggested that a larger index is an indication of an isotropic core contraction that is not likely regulated by magnetic fields. Several observational studies of resolved

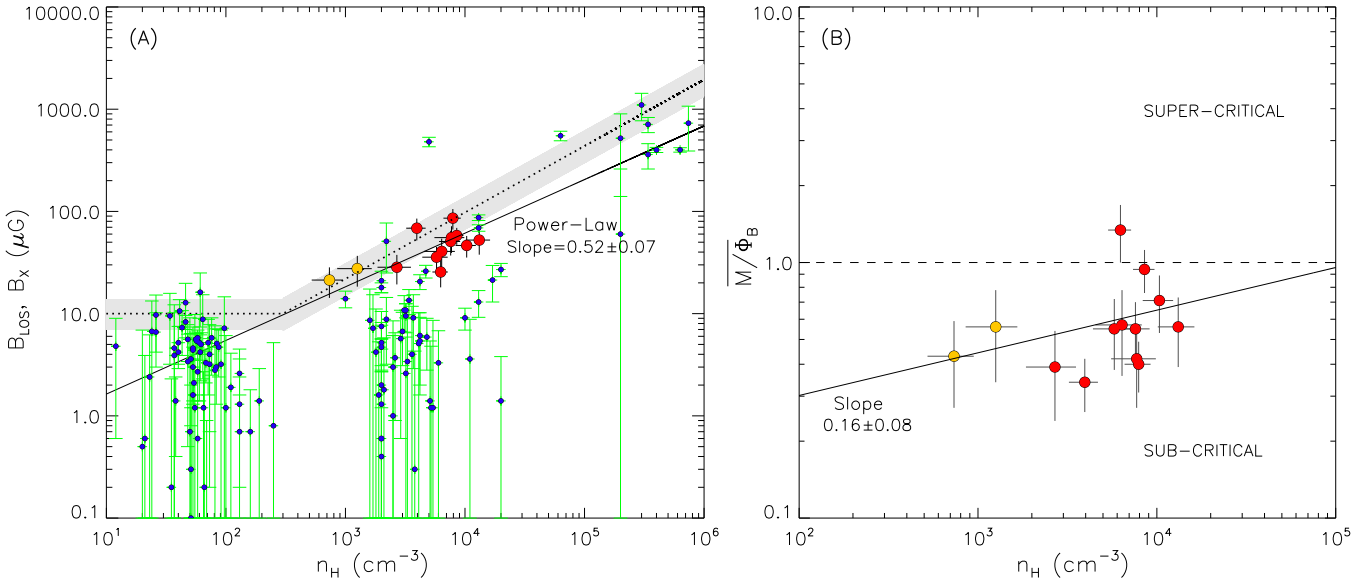

Figure 15. Panel (A): log–log plot of one-dimensional magnetic field strength (B_X) against atomic hydrogen volume density ($n_H = 2\,n_{H_2}$) for clumps (red points) and diffuse regions (yellow points) of the S235 complex. B_X is obtained by scaling B_{pos} by $1/\sqrt{2}$. The B_{LOS} values and limits from Crutcher et al. (2010) are shown as blue points with green error bars. The dotted black line with gray shading (index of 0.65) shows the maximum B_{LOS} with 1σ uncertainties for the Crutcher et al. (2010) Bayesian analysis. The solid black line shows the single power-law fit to the S235 values, which gives an index of $\kappa = 0.52 \pm 0.07$. Panel (B): log–log plot of normalized mass-to-flux ratio ($\overline{M/\Phi_B}$) vs. atomic hydrogen volume density for the S235 clumps (red points) and diffuse regions (yellow points). The black dashed line represents unity in $\overline{M/\Phi_B}$, differentiating subcritical and supercritical states. A single power-law fit to the values gives a slope of 0.16 ± 0.08 and is shown by the solid black line.

magnetic field maps of individual clouds have found higher indices of ∼0.7 (Marchwinski et al. 2012; Hoq et al. 2017).

Here, the S235 clumps show a power-law scaling in the relation between mean one-dimensional magnetic field strength ($B_X = B_{pos}/\sqrt{2}$) and atomic gas number density (n_H), as shown in Figure 15(A). A single power-law fit gives a slope of $\kappa = 0.52 \pm 0.07$. This slope is shallower than the 0.65 index of Crutcher et al. (2010) and implies that the S235 clumps are likely influenced by magnetic fields. Li et al. (2015) studied magnetic field properties in NGC 6334 from scales of 0.01–10 pc. They obtained a slope of $\kappa = 0.41$ and suggested that molecular fragmentation is anisotropic, with magnetic fields playing a crucial role in that cloud fragmentation. Wang et al. (2020) carried out a detailed study of the IC5146 cloud using a Bayesian approach and found a slope of $\kappa = 0.5$. They also found that the probability density function for having a strong magnetic field strength was narrow and Gaussian. The S235 slope correlates well with the aforementioned studies and demonstrates that the S235 clumps are likely regulated by magnetic fields through ambipolar diffusion.

One of the important predictions of the ambipolar diffusion mechanism is the increase in the mass-to-flux ratio from the subcritical to the supercritical state with increasing density (Mouschovias 1991; Mouschovias & Ciolek 1999). This occurs since the drift of neutral gas into the core increases the density of the region without an equally significant increase in the magnetic flux. We compared $\overline{M/\Phi_B}$ against n_H for the S235 regions as shown in Figure 15(B). There is a positive correlation between both quantities with clumps that are more dense tending to have higher $\overline{M/\Phi_B}$. A single power-law fit gives a slope of 0.16 ± 0.08. Extrapolating the slope (not shown in the figure), we infer a change of $\overline{M/\Phi_B}$ from subcritical to supercritical for densities greater than 10^5 cm^{-3}. At these large densities, most of the gas exists as dense cores that are gravitationally unstable and in turn have supercritical states. A similar study was carried out by Hoq et al. (2017) for the G28.23 dark cloud; they found the critical density to be around 300–600 cm^{-3}, which is comparable to densities found in semi-diffuse molecular regions. Heitsch & Hartmann (2014) showed that the transition from subcritical to supercritical is more efficient at high densities and on dense core size scales.

The main concern with star formation solely regulated by ambipolar diffusion is derived from the comparison of triggered star formation timescales with ambipolar diffusion timescales. The latter process gives rise to slow star formation (Shu et al. 1987), which appears inconsistent with the typical ages of YSOs in molecular clouds (Hartmann et al. 2001). Instead, accretion, along magnetic field lines, but via shocks, appears to be a likely mechanism to tip cores over from being subcritical to supercritical (Heitsch & Hartmann 2014). Moreover, turbulent magnetic reconnection (Lazarian & Vishniac 1999; Lazarian et al. 2012), although suggested as a means of speeding up the star formation process, also appears too slow. Hence, the triggered star formation in S235 is more likely the combination of shock compression, turbulent motions, and ambipolar diffusion.

6. Conclusions

We have studied the magnetic field properties in the S235 complex using new NIR *H*-band starlight polarimetric observations in combination with archival 1.1 mm dust continuum emission, ^{13}CO molecular spectral line data, and Planck polarized dust emission. The main results of the study are as follows:

1. The POS magnetic field orientations were traced using 375 bona fide embedded and background starlight polarization measurements. The contributing stars were selected through the evaluation of Gaia DR2 distances and extinctions derived from 2MASS and UKIDSS

colors. The magnetic field orientations showed a curved morphology outlining the (spherical) shell created by the central star's ionized emission. This indicates that the magnetic field coupled with the gas is pushed by the expansion of the H II region.

2. The large-scale magnetic field orientation inferred from Planck data was found to be mostly parallel to the Galactic plane.
3. We identified 11 dense clumps in the S235 complex using 1.1 mm dust emission. The clump masses were estimated to be 33–525 $M_{\odot}$, with clump-averaged H_2 column densities of about 6.9×10^{21} cm^{-2}. The ^{13}CO spectral line data traced the S235 cloud in the velocity range -25 to -15 km s^{-1}, with the projected distributions of molecular gas and dust emission showing clear associations.
4. We estimated the POS magnetic field strength for the clumps using the Davis and Chandrashekar–Fermi method. The values ranged between 36 and 121 μG. The estimated mass-to-flux ratios show the clumps to be magnetically subcritical ($\overline{M/\Phi_B} \sim 0.6$). The turbulent Alfvén Mach number and plasma beta were also found to be less than unity ($\mathcal{M}_A \sim 0.5$, $\beta_p \sim 0.04$), indicating a strongly magnetized region.
5. The dust grain alignment with respect to the local magnetic field was studied through analysis of polarization efficiency. The observations reveal a negative power-law dependence for polarization efficiency versus extinction, with an index of -0.66 ± 0.08. These results favor the RAT theory and indicate that background starlight polarization traces the magnetic field within the clumps.
6. Comparison of magnetic field strength with density shows a power-law dependence, with an index of 0.52 ± 0.07. This is consistent with values obtained for strong field models driven by ambipolar diffusion cloud contraction. The dependence of the mass-to-flux ratio on density shows a positive correlation, with an $\overline{M/\Phi_B}$ change from subcritical to supercritical for densities greater than 10^5 cm^{-3}. These results further confirm the predictions of strongly magnetized cloud evolution.

In summary, the S235 complex is revealed to be a strongly magnetized region in which the expansion of an H II region influences the magnetic field orientations. The star formation history indicates that stellar feedback may have initially played a positive role in triggering new stars. However, as the H II region evolved, the magnetic fields become dynamically important enough to regulate later global star formation.

The authors would like to thank the anonymous referee for a detailed and thoughtful review that has improved the scientific content of the paper. This research has been supported by the European Research Council advanced grant H2020-ER-2016-ADG-743029 under the European Unions Horizon 2020 Research and Innovation program. R.D. acknowledges INAOE and CONACyT-Mexico for Sistema Nacional de Investigadores (SNI) grant (CVU 555629). A.L. acknowledges financial support by CONACyT-Mexico through project CB-A1S54450. J.M. acknowledges funding from a Royal Society-SFI University Research Fellowship (14/RS-URF/3219). We thank all of the OAGH staff for their help in conducting observations with POLICAN. This research was conducted in part using the Mimir instrument, jointly developed at Boston University and Lowell Observatory and supported by NASA, NSF, and the W. M. Keck Foundation. The analysis software for Mimir data was developed under NSF grants AST 06-07500, 09-07790, 14-12269, and 18-14531 to Boston University. This work makes use of data products from the Two Micron All Sky Survey, which is a joint project of the University of Massachusetts and the Infrared Processing and Analysis Center/California Institute of Technology, funded by NASA and NSF. The authors acknowledge the use of SAOImage DS9 software, which was developed with funding from the Chandra X-ray Science Center, the High Energy Astrophysics Science Archive Center, and JWST Mission office at Space Telescope Science Institute.

ORCID iDs

R. Devaraj https://orcid.org/0000-0001-9217-3168
D. P. Clemens https://orcid.org/0000-0002-9947-4956
L. K. Dewangan https://orcid.org/0000-0001-6725-0483
A. Luna https://orcid.org/0000-0002-3922-6168
T. P. Ray https://orcid.org/0000-0002-2110-1068
J. Mackey https://orcid.org/0000-0002-5449-6131

References

Aguirre, J. E., Ginsburg, A. G., Dunham, M. K., et al. 2011, ApJS, 192, 4
Alves, F. O., Frau, P., Girart, J. M., et al. 2014, A&A, 569, L1
Anderson, L. D., Makai, Z., Luisi, M., Andersen, M., et al. 2019, ApJ, 882, 11
Andersson, B.-G., Lazarian, A., & Vaillancourt, J. E. 2015, ARA&A, 53, 501
Arce, H. G., Goodman, A. A., Bastien, P., Manset, N., & Sumner, M. 1998, ApJL, 499, L93
Arthur, S. J., Henney, W. J., Mellema, G., de Colle, F., et al. 2011, MNRAS, 414, 1747
Bailer-Jones, C. A. L., Rybizki, J., Fouesneau, M., Mantelet, G., & Andrae, R. 2018, AJ, 156, 58
Bally, J., Aguirre, J., Battersby, C., et al. 2010, ApJ, 721, 137
Bastien, P. 1996, in ASP Conf. Ser. 97, Polarimetry of the Interstellar Medium, ed. W. G. Roberge & D. C. B. Whittet (San Francisco, CA: ASP), 297
Battersby, C., Bally, J., Jackson, J., et al. 2010, ApJ, 721, 222
Beck, R. 2015, A&ARv, 24, 4
Beck, R., Brandenburg, A., Moss, D., et al. 1996, ARA&A, 34, 155
Bertoldi, F. 1989, ApJ, 346, 735
Bessell, M. S., & Brett, J. M. 1988, PASP, 100, 1134
Bieging, J. H., Patel, S., Peters, W. L., Viktor Toth, L., et al. 2016, ApJS, 226, 13
Bisbas, T. G., Wunsch, R., Whitworth, A. P., & Hubber, D. A. 2011, ApJ, 736, 142
Bourke, T., Myers, P., Robinson, G., & Hyland, A. 2001, ApJ, 554, 916
Brown, A. G. A., Vallenari, A., Prusti, T., et al. 2018, A&A, 616, A1
Brunt, C. 2004, in Proc. of ASP Conf. Ser. 317, Milky Way Surveys: The Structure and Evolution of our Galaxy, ed. D. Clemens, R. Shah, & T. Brainerd (San Francisco, CA: ASP), 79
Burns, R. A., Imai, H., Handa, T., et al. 2015, MNRAS, 453, 3163
Camargo, D., Bonatto, C., & Bica, E. 2011, A&A, 416, 1522
Carpenter, J. M. 2001, AJ, 121, 2851
Carrasco, L., Hernández Utrera, O., Vázquez, S., et al. 2017, RMxAA, 53, 497
Cashman, L. R., & Clemens, D. P. 2014, ApJ, 793, 126
Chandrasekhar, S., & Fermi, E. 1953, ApJ, 118, 113
Chapman, N. L., Goldsmith, P. F., Pineda, J. L., & Clemens, D. P. 2011, ApJ, 741, 21
Chavarría, L., Allen, L., Brunt, C., et al. 2014, MNRAS, 439, 3719
Chen, Z., Jiang, Z., Tamura, M., Kwon, J., & Roman-Lopes, A. 2017, ApJ, 838, 80
Churchwell, E., Povich, M. S., Allen, D., et al. 2006, ApJ, 649, 759
Clemens, D. P., Cashman, L. R., Cerny, C., El-Batal, A. M., et al. 2020, ApJS, 249, 23
Clemens, D. P., El-Batal, A. M., Cerny, C., Kressy, S., et al. 2018, ApJ, 867, 79
Clemens, D. P., Pinnick, A., & Pavel, M. D. 2012b, ApJS, 200, 20
Clemens, D. P., Pinnick, A., Pavel, M. D., & Taylor, B. W. 2012a, ApJS, 200, 19

Clemens, D. P., Sarcia, D., Grabau, A., et al. 2007, PASP, 119, 1385
Cohen, J. G., Persson, S. E., Elias, J. H., & Frogel, J. A. 1981, ApJ, 249, 481
Crutcher, R. M. 1999, ApJ, 520, 706
Crutcher, R. M. 2012, ARA&A, 50, 29
Crutcher, R. M., Nutter, D. J., Ward-Thompson, D., et al. 2004, ApJ, 600, 279
Crutcher, R. M., Wandelt, B., Heiles, C., Falgarone, E., & Troland, T. 2010, ApJ, 725, 466
Davis, L. 1951, PhRvL, 81, 890
Deharveng, L., Schuller, F., Anderson, L. D., et al. 2010, A&A, 523, 6
Deharveng, L., Zavagno, A., & Caplan, J. 2005, A&A, 433, 565
Devaraj, R., Luna, A., Carrasco, L., et al. 2018a, PASP, 130, 055002
Devaraj, R., Mayya, Y. D., Carrasco, L., & Luna, A. 2018b, PASP, 130, 055001
Dewangan, L. K., & Anandarao, B. G. 2011, MNRAS, 414, 1526
Dewangan, L. K., Devaraj, R., & Ojha, D. K. 2018, ApJ, 854, 106
Dewangan, L. K., & Ojha, D. K. 2017, ApJ, 849, 65
Dewangan, L. K., Ojha, D. K., Anandarao, B. G., Ghosh, S. K., & Chakraborti, S. 2012, ApJ, 756, 151
Dewangan, L. K., Ojha, D. K., Luna, A., et al. 2016, ApJ, 819, 66
Dunham, M. K., Rosolowsky, E., Evans, N. J., II, Cyganowski, C., & Urquhart, J. S. 2011, ApJ, 741, 110
Elmegreen, B. G., & Lada, C. J. 1977, ApJ, 214, 725
Enoch, M. L., Young, K. E., Glenn, J., et al. 2006, ApJ, 638, 293
Evans, N. J., II 1999, ARA&A, 37, 311
Evans, N. J., II, & Blair, G. N. 1981, ApJ, 246, 394
Fazio, G. G., Hora, J. L., Allen, L. E., et al. 2004, ApJS, 154, 10
Felli, M., Massi, F., Navarrini, A., et al. 2004, A&A, 420, 553
Felli, M., Massi, F., Robberto, M., & Cesaroni, R. 2006, A&A, 453, 911
Felli, M., Testi, L., Valdettaro, R., & Wang, J.-J. 1997, A&A, 320, 594
Ferland, G. J. 2009, in IAU Symp. 259, Cosmic Magnetic Fields: From Planets, to Stars and Galaxies, ed. K. G. Strassmeier, A. G. Kosocichev, & J. Beckmann (Cambridge: Cambridge Univ. Press), 25
Ferrière, K. 2011, MmSAI, 82, 824
Fiedler, R., & Mouschovias, T. 1993, ApJ, 415, 680
Georgelin, Y. M., Georgelin, Y. P., & Roux, S. 1973, A&A, 25, 337
Ginsburg, A., Glenn, J., Rosolowsky, E., et al. 2013, ApJS, 208, 14
Hall, J. S. 1949, Sci, 109, 166
Hartmann, L., Ballesteros-Paredes, J., & Bergin, E. A. 2001, ApJ, 562, 852
Heiles, C., & Crutcher, R. 2005, Cosmic Magnetic Fields (Berlin: Springer), 137
Heitsch, F., & Hartmann, L. 2014, MNRAS, 443, 230
Heitsch, F., Zweibel, E. G., Mac Low, M.-M., Li, P., & Norman, M. L. 2001, ApJ, 561, 800
Heyer, M. H., Carpenter, J. M., & Ladd, E. F. 1996, ApJ, 463, 630
Hildebrand, R. H. 1983, QJRAS, 24, 267
Hiltner, W. A. 1949, ApJ, 109, 471
Hoang, T., & Lazarian, A. 2008, MNRAS, 388, 117
Hodgkin, S. T., Irwin, M. J., Hewett, P. C., & Warren, S. J. 2009, MNRAS, 394, 675
Hoq, S., Clemens, D. P., Guzman, A. E., & Cashman, L. R. 2017, ApJ, 836, 199
Jackson, J. M., Rathborne, J. M., Shah, R. Y., et al. 2006, ApJS, 163, 145
Johnstone, D., & Bally, J. 2006, ApJ, 653, 383
Kauffmann, J., Bertoldi, F., Bourke, T. L., Evans, N. J., II, & Lee, C. W. 2008, A&A, 487, 993
Kirsanova, M. S., Boley, P. A., Moiseev, A. V., Wiebe, D. S., & Uklein, R. I. 2020, MNRAS, 497, 1050
Kirsanova, M. S., Sobolev, A. M., Thomasson, M., et al. 2008, MNRAS, 388, 729
Kirsanova, M. S., Wiebe, D. S., Sobolev, A. M., et al. 2014, MNRAS, 437, 1593
Krumholz, M. R., & Federrath, C. 2019, FrASS, 6, 7
Krumholz, M. R., Stone, J. M., & Gardiner, T. A. 2007, ApJ, 671, 518
Kusune, T., Sugitani, K., Miao, J., et al. 2015, ApJ, 798, 60
Lada, C. J., & Adams, F. C. 1992, ApJ, 393, 278
Lawrence, A., Warren, S. J., Almaini, O., et al. 2007, MNRAS, 379, 1599
Lazarian, A., Esquivel, A., & Crutcher, R. M. 2012, ApJ, 757, 154
Lazarian, A., & Hoang, T. 2007, MNRAS, 378, 910
Lazarian, A., & Vishniac, E. T. 1999, ApJ, 517, 700
Li, H.-B., Goodman, A., Sridharan, T. K., et al. 2014, in Protostars and Planets VI, ed. H. Beuther et al. (Tuscon, AZ: Univ. Arizona Press), 101
Li, H.-B., Yuen, K. H., Otto, F., Leung, P. K., et al. 2015, Natur, 520, 518
Li, T., Li, P.-S., Juvela, M., Kim, K. T., Evans, N. J., II, et al. 2018, ApJ, 859, 151
Mackey, J., & Lim, A. J. 2011, MNRAS, 412, 2079
Mallick, K. K., Ojha, D. K., Samal, M. R., Pandey, A. K., et al. 2012, ApJ, 759, 48
Marchwinski, R. C., Pavel, M. D., & Clemens, D. P. 2012, ApJ, 755, 130
Martin, P. G., Adamson, A. J., Whittet, D. C. B., et al. 1992, ApJ, 392, 691
Mathewson, D. S., & Ford, V. L. 1970, MmRAS, 74, 139
Mathis, J. S. 1990, ARA&A, 28, 37
McKee, C. F., & Ostriker, E. C. 2007, ARA&A, 45, 565
McKee, C. F., & Tan, J. C. 2003, ApJ, 585, 850
Mestel, L., & Spitzer, L., Jr. 1956, MNRAS, 116, 505
Meyer, M. R., Calvet, N., & Hillenbrand, L. A. 1997, AJ, 114, 288
Mouschovias, T. C. 1991, ApJ, 373, 169
Mouschovias, T. C., & Ciolek, G. E. 1999, in The Origin of Stars and Planetary Systems, ed. C. J. Lada & N. D. Kylafis, 540 (Amsterdam: Kluwer Academic Publishers), 305
Mouschovias, T. C., & Spitzer, L., Jr. 1976, ApJ, 210, 326
Mouschovias, T. C., Tassis, K., & Kunz, M. W. 2006, ApJ, 646, 1043
Mueller, K. E., Shirley, Y. L., Evans, N. J., II, et al. 2002, ApJS, 143, 469
Nakamura, F., & Li, Z.-Y. 2008, ApJ, 687, 354
Ostriker, E. C., Stone, J. M., & Gammie, C. F. 2001, ApJ, 546, 980
Padoan, P., Goodman, A., Draine, B. T., et al. 2001, ApJ, 559, 1005
Padoan, P., Jimenez, R., Juvela, M., & Nordlund 2004, ApJL, 604, L49
Pillai, T., Kauffmann, J., Wyrowski, F., et al. 2011, A&A, 530, A118
Planck Collaboration I 2016, A&A, 594, A1
Planck Collaboration VIII 2016, A&A, 594, A8
Planck Intermediate Results XXXIV 2016, A&A, 586, A137
Rieke, G. H., & Lebofsky, M. J. 1985, ApJ, 288, 618
Rosolowsky, E., Dunham, M. K., Ginsburg, A., Bradley, T. E., et al. 2010, ApJS, 188, 123
Santos, F. P., Ade, P. A. R., Angile, F. E., et al. 2017, ApJ, 837, 161
Santos, F. P., Franco, G. A. P., Roman-Lopes, A., et al. 2014, ApJ, 783, 1
Sharpless, S. 1959, ApJS, 4, 257
Shu, F. H., Adams, F. C., & Lizano, S. 1987, ARA&A, 25, 23
Simon, R., Jackson, J. M., Clemens, D. P., et al. 2001, ApJ, 551, 747
Skrutskie, M. F., Cutri, R. M., Stiening, R., et al. 2006, AJ, 131, 1163
Sugitani, K., Tamura, M., Nakajima, Y., Nagashima, C., et al. 2002, ApJ, 565, L25
Tamura, M., Kandori, R., Kusakabe, N., et al. 2006, ApJ, 649, L29
Tan, J. C., Beltran, M. T., Caselli, P., et al. 2014, in Protostars and Planets VI, ed. H. Beuther et al. (Univ. Arizona Press), 149
Tang, Y.-W., Ho, P. T. P., Girart, J. M., et al. 2009, ApJ, 695, 1399
Thompson, M. A., Urquhart, J. S., Moore, T. J. T., & Morgan, L. K. 2012, MNRAS, 421, 408
Troland, T., & Crutcher, R. 2008, ApJ, 680, 457
Wang, J.-W., Lai, S.-P., Clemens, D. P., Koch, P. M., et al. 2020, ApJ, 888, 13
Wang, J.-W., Lai, S.-P., Eswaraiah, C., Clemens, D. P., et al. 2017, ApJ, 849, 157
Wardle, J. F. C., & Kronberg, P. P. 1974, ApJ, 194, 249
Werner, M. W., Roellig, T. L., Low, F. J., Rieke, G. H., et al. 2004, ApJS, 154, 1
Whittet, D. C. B., Hough, J. H., Lazarian, A., & Hoang, T. 2008, ApJ, 674, 304
Whittet, D. C. B., Martin, P. G., Hough, J. H., et al. 1992, ApJ, 386, 562
Yoo, T. S. (ed.) 2004, Insight Into Images 1st Edition (New York: A K Peters/CRC Press)
Zinnecker, H., & Yorke, H. W. 2007, ARA&A, 45, 481